



저작자표시-비영리-변경금지 2.0 대한민국

이용자는 아래의 조건을 따르는 경우에 한하여 자유롭게

- 이 저작물을 복제, 배포, 전송, 전시, 공연 및 방송할 수 있습니다.

다음과 같은 조건을 따라야 합니다:



저작자표시. 귀하는 원저작자를 표시하여야 합니다.



비영리. 귀하는 이 저작물을 영리 목적으로 이용할 수 없습니다.



변경금지. 귀하는 이 저작물을 개작, 변형 또는 가공할 수 없습니다.

- 귀하는, 이 저작물의 재이용이나 배포의 경우, 이 저작물에 적용된 이용허락조건을 명확하게 나타내어야 합니다.
- 저작권자로부터 별도의 허가를 받으면 이러한 조건들은 적용되지 않습니다.

저작권법에 따른 이용자의 권리는 위의 내용에 의하여 영향을 받지 않습니다.

이것은 [이용허락규약\(Legal Code\)](#)을 이해하기 쉽게 요약한 것입니다.

[Disclaimer](#)

이학박사 학위논문

**Structural analysis of AdipoR1-P5
complex model and mitochondrial
creatine kinase heteromeric complex**

AdipoR1-P5 복합체 모델 및 미토콘드리아 크레아틴

키나제 이종 복합체의 구조 분석

2024 년 2 월

서울대학교 대학원

화학부 구조생화학 전공

빈 경 욱

Structural analysis of AdipoR1-P5 complex model and mitochondrial creatine kinase heteromeric complex

지도 교수 이형호

이 논문을 이학박사 학위논문으로 제출함

2024년 2월

서울대학교 대학원
화학부 구조생화학 전공
빈경욱

빈경욱의 이학박사 학위논문을 인준함

2023년 12월

위원장 이현우 (인)

부위원장 이형호 (인)

위원 이연 (인)

위원 최희정 (인)

위원 우재성 (인)

Abstract

Structural analysis of AdipoR1-P5 complex model and mitochondrial creatine kinase heteromeric complex

Kyung Wook Been
Department of Chemistry
The Graduate School
Seoul National University

The dissertation mainly focuses on gaining a molecular level of understanding of how ligands bind and solving structure of proteins with novel properties in cellular environment. The dissertation is divided into two research chapters.

In **chapter 1**, the structural analysis of the adiponectin receptor 1-pentapeptide (AdipoR1-P5) model will be discussed. AdipoR1 is a GPCR-like receptor and mediates AMP-activated protein kinase (AMPK) signaling pathway when adiponectin (APN) binds. The apo-structure of AdipoR1 was reported in 2015, but the structure of AdipoR1-APN complex has not yet been solved. Although it is necessary to create an optimal agonist to treat APN-related diseases based on the structural information of

the AdipoR1-APN complex, the interaction between AdipoR1 and APN is still unknown. Therefore, I analyzed the AdipoR1-APN complex model to determine how APN binds to AdipoR1 and the binding site of APN that binds to AdipoR1. Herein, I found a small region (P5; GLYYF), which is derived from the original sequence of endogenous APN using multiple sequence alignment and molecular docking simulation. Additionally, I demonstrated that it could function as an efficient ligand for AdipoR1 by providing the AdipoR1-P5 complex model. In doing this, I elucidated a crucial key amino acid sequence for the binding between AdipoR1 and APN, which could be applied in a strategy to discover new candidate drug by designing AdipoR1 activating peptides.

In **chapter 2**, the structural and functional studies of mitochondrial creatine kinase (CKMT1 and CKMT2) will be discussed. This study was initiated based on the previous results with analyzing 369 cancer cell line proteome data provided by Steven P. Gygi's group. Interestingly, I discovered two proteins, which is CKMT1 and CKMT2 located in mitochondria, with high Pearson's correlation values. Although it has been known that the tissues in which CKMT1 and CKMT2 are expressed are different, the high Pearson's correlation value suggests that the two proteins can interact with each other to perform biological functions in cells. So, I hypothesized that CKMT1 and CKMT2 would form a heteromeric complex and function in the mitochondria. Accordingly, I determined X-ray crystal

structure of CKMT heteromeric complex and verified that it forms an octamer with 4:4 stoichiometry. Interestingly, the heteromeric complex was found to have different properties from the previously reported homomeric complex. In particular, the heteromeric complex had better thermal stability than the homomeric complex. Based on our experimental data, our findings indicate the potential formation of a CKMT heteromeric complex with high expression correlation value and high thermal stability. Recently, more quantitative proteomics revealed that CKMT1 and CKMT2 were strongly upregulated in thermogenic adipocytes. In this context, our studies could suggest significant biological implications relevant to heat generating environment in tissues.

Keyword: Adiponectin receptor 1, pentapeptide, molecular docking simulation, mitochondrial creatine kinase, X-ray crystallography, thermostability

Student Number: 2016-20347

Table of Contents

Chapter 1. Structural analysis of AdipoR1-P5 model

1.1. Introduction.....	14
1.1.1. Background of APN and AdipoRs.....	14
1.1.2. Limitations of APN as a agonist and mimetic peptides.....	18
1.1.3. AdipoR1-related disease : hair loss	20
1.2. Materials and Methods	22
1.2.1. Protein sequence database, MSA, conserved score calculation, and structure visualization	22
1.2.2. 3-(4,5-dimethylthiazole-2-yl)-2,5-diphenyltetrazolium bromide (MTT assay)	22
1.2.3. Expression and purification of GST-fused pentapeptide	23
1.2.4. Pulldown assay	23
1.2.5. Molecular docking of P5 to AdipoR1	24
1.2.6. RNA interference for AdipoR1	25
1.2.7. Mouse hair cycle modulation	26
1.3. Results.....	31
1.3.1. Two potential small 5-mer peptides are positioned within a highly conserved sequence of APN	31

1.3.2. P5 directly binds with AdipoR1	35
1.3.3. Structural analysis of the specific binding pocket of AdipoR1 for P5	41
1.3.4. P5 activates AMPK signaling pathway through AdipoR1 in ORS and DP cells	50
1.3.5. Topical P5 treatment induced the anagen hair cycle <i>in vivo</i>	52
1.4. Discussion	54
1.5. Reference	57

Chapter 2. Structural insights into the functions and assembly of mitochondrial creatine kinase

2.1. Introduction.....	67
2.1.1. Background of CKMT	67
2.1.2. Expression correlation of CKMT1 and CKMT2.....	72
2.1.3. Creatine-dependent thermogenesis.....	74
2.2. Materials and methods.....	77
2.2.1. Expression and purification of CKMT	77
2.2.2. In gel digestion and mass spectrometry analysis.....	78
2.2.3. Negative staining	79
2.2.4. Western blot analysis	79
2.2.5. X-ray data collection and refinement	79
2.2.6. Dynamic light scattering.....	82
2.2.7. Creatine kinase activity and co-operativity analysis	82
2.3. Results.....	84
2.3.1. Purification and identification of WT CKMT and W213A CKMT heteromeric complex	84
2.3.2. Overall structure of the CKMT heteromeric complex.....	92
2.3.3. Characterization of the CKMT heteromeric complex	99

2.3.4. Structural perspective on the reason for the high thermal stability of CKMT heteromeric complex.....	104
2.4. Discussion	112
2.5. Reference	114
Abstract in Korea (국문초록)	120
Acknowledgement	123

Figure Contents

Chapter 1. Structural analysis of AdipoR1-P5 model

Figure 1.1 APN and AdipoRs.	16
Figure 1.2 Topology and signaling pathway of AdipoRs	17
Figure 1.3 Construct design used in the experiment.....	27
Figure 1.4 GST affinity purification of GST-fused pentapeptide	28
Figure 1.5 Excavation of the most conserved residues in APN Globular domain.....	33
Figure 1.6 The screening of candidate 5-mer peptides based on DP and ORS cell proliferation.....	34
Figure 1.7 Direct molecular interaction between the P5 and AdipoR1	37
Figure 1.8 P5 binds to both full-length AdipoR1 and N-terminal -truncated AdipoR1	38
Figure 1.9 The colocalization of P5 and AdipoR1 <i>in vitro</i>	39
Figure 1.10 The position of P5 in APN	40
Figure 1.11 The most optimal docking model for the AdipoR1-P5 complex	44
Figure 1.12 Sequence logo landscape of MSA of extracellular loop 2 of AdipoR1	45
Figure 1.13 Cartoon diagram of the superposition of APN with the Docking model of the AdipoR1-P5 complex	46

Figure 1.14 Mutational studies based on molecular docking simulation	47
Figure 1.15 Pulldown of AdipoR1 mutant (residues 89-375) with the GST-fused P5.....	48
Figure 1.16 Pulldown of AdipoR1 (residues 89-375) with GST-P5 or GST fused to two mutant peptide (GLYDF and (GLYAF). ..	49
Figure 1.17 P5 activate AMPK signaling pathway through AdipoR1 in vitro.....	51
Figure 1.18 Topical P5 treatment induced the anagen hair cycle through AdipoR1 in vivo	53

Chapter 2. Structural insights into the functions and assembly of mitochondrial creatine kinase

Figure 2.1 Role of CKMT in high energy metabolite transport and cellular respiration	69
Figure 2.2 Molecular architecture of CKMT.....	70
Figure 2.3 CKMT residues involved in octamer stability	71
Figure 2.4 Expression correlation of CKMT1 and CKMT2.....	73
Figure 2.5 Creatine cycling model.....	76
Figure 2.6 Schematic diagram for expression and purification of CKMT heteromeric complex.....	86
Figure 2.7 Purification of CKMT heteromeric complex and negative staining experiment	87
Figure 2.8 Representative LC-MS/MS spectrum of CKMT heteromeric complex	88
Figure 2.9 Sequence alignment of human CKMT1 and CKMT2	89
Figure 2.10 Sequence alignment of residues 207-219 of CKMT1 and CKMT2	90
Figure 2.11 Purification of W213A CKMT heteromeric complex, negative staining experiment and creatine kinase activity test.....	91
Figure 2.12 Comparison of electron density map of residue 213 of CKMT1 and CKMT2, and CKMT heteromeric complex octamer structure	

.....	94
Figure 2.13 Schematic representation of the secondary structure of CKMT	95
Figure 2.14 X-ray crystal structure of W213A CKMT heteromeric complex	96
Figure 2.15 Superimposed structures of heteromeric dimer and homomeric dimer.....	97
Figure 2.16 Comparison of octamer structures of CKMT.....	98
Figure 2.17 Functional characterization of CKMT in vitro.....	101
Figure 2.18 Thermal stability of CKMT complexes.....	102
Figure 2.19 Thermal stability of CKMT complexes at 42 and 48°C, and a change in the kinase activity depending on time	103
Figure 2.20 Sequence alignment and structure comparison of N-terminus	106
Figure 2.21 Chimera construct design and thermal stability of chimera heteromeric complex	108
Figure 2.22 Interactions and hydrophobicity of residues round W264 ..	109
Figure 2.23 Dimer-dimer interface of heteromeric complex and thermal stability of R151A heteromeric complex	110
Figure 2.24 Dimer-dimer interface of CKMT1 and CKMT2 homomeric complex	111

Table Contents

Table 1.1 Published small molecules and mimetic peptides	
activating AdipoRs	19
Table 1.2 Sequence for site-directed mutagenesis	29
Table 2.1 Statistic for data collection and refinement.....	81

Chapter 1.

Structural analysis of AdipoR1-P5 model

Data produced by other groups is included in this chapter.

Published in *EMBO Molecular Medicine*

Jungyoon Ohn[#], Kyung Wook Been[#], Jin Yong Kim[#], Eun Ju Kim[#], Taeyong Park, Hye-Jin Yoon, Jeong Seok Ji, Miki Okada-Iwabu, Masato Iwabu, Toshimasa Yamauchi, Yeon Kyung Kim, Chaok Seok, Ohsang Kwon, Kyu Han Kim, Hyung Ho Lee* and Jin Ho Chung*, "Discovery of transdermally deliverable pentapeptide for activating AdipoR1 to promote hair growth", *EMBO Molecular Medicine* (2021) ([#]co-first author)

<https://doi.org/10.15252/emmm.202013790>

1.1. Introduction

1.1.1. Background of APN and AdipoRs

APN is a protein isolated from adipose tissue that contains 244 amino acids with a molecular weight of 28 kDa in humans (Nakano et al, 1996). APN consists of four structural domains: a N-terminal signal peptide, a hypervariable domain, a collagenous domain, and a C-terminal globular domain, with the globular domain being biologically active (Wong et al, 2004). APN circulates in human plasma as multimers and binds to two types of AdipoRs (**Figure 1.1**). The assembly is carried out in the endoplasmic reticulum by post-translational modifications, such as hydroxylations and glycosylations of the APN monomer (Wang et al, 2008). The globular domain allows the formation of low molecular weight trimers via hydrophobic bonds, and disulfide bond interactions at the collagen domain allow the formation of medium molecular weight hexamers (association of two trimers) and high molecular weight multimers (4 to 6 trimers) (Waki et al, 2003; Tsao et al, 2003; Pajvani et al, 2003). APN is also present in plasma in its globular form alone, resulting from proteolysis, but in very small quantities (Fruebis et al, 2001). The different forms of APN have different biological properties and probably different tissue targets.

APN requires binding to its receptors in order to have a biological impact. The AdipoR1 and AdipoR2 receptors were first identified by Yamauchi et al.

(2003). These receptors belong to the superfamily of AdipoQ and progestin receptors, which has seven transmembrane helices. They have an internal N-terminus and an extracellular-C terminus, which is the reverse topology of all other G protein coupled receptors. (Yamauchi et al, 2003) (**Figure 1.2A**). The globular form is preferred by the AdipoR1 receptor, while the high molecular weight form is preferred by the AdipoR2 receptor. Mice studies have demonstrated that these two receptors are the primary APN receptors *in vivo* and they mediate APN actions (Yamauchi et al, 2007). Thus, KO mice for these two receptors develop glucose intolerance and hyperinsulinemia, demonstrating their importance in carbohydrate homeostasis and insulin sensitivity. These effects appear to be receptor specific, with AdipoR1 being engaged in AMPK activation whereas AdipoR2 is involved in PPAR activation (Yamauchi et al, 2014) (**Figure 1.2B**). Accordingly, the study investigating these receptors discovered that the roles of the AdipoR1 and AdipoR2 receptors in metabolism are quite distinct.

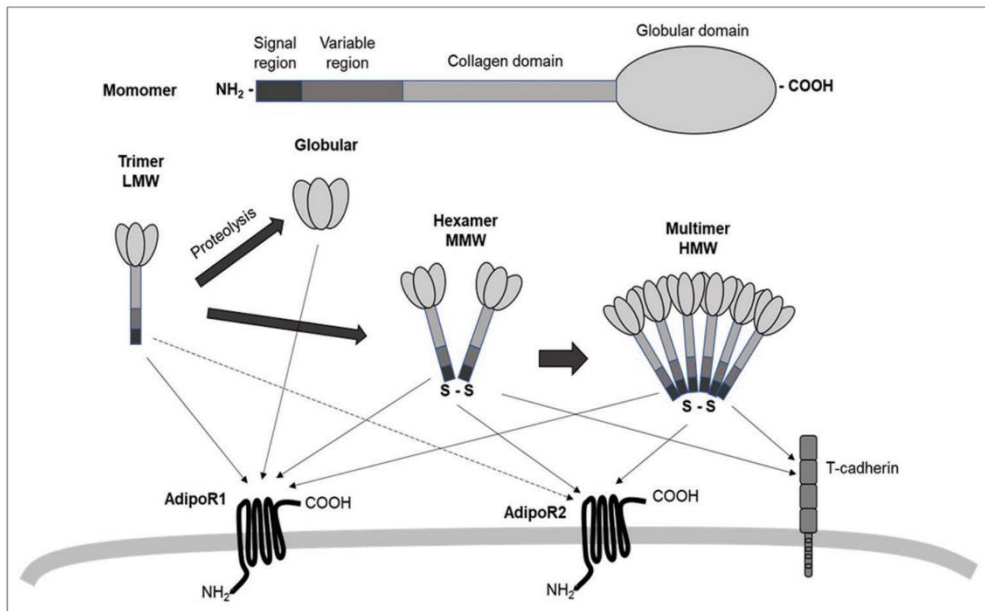


Figure 1.1 APN and AdipoR

Monomeric APN consists of a signal peptide, a variable region, a collagen domain, and a globular domain. Oligomerization facilitates the formation of the trimers (LMW), hexamers (MMW), and multimer (HMW). APN interacts with AdipoR1 and AdipoR2. This figure is adapted from Thi Mong Diep Nguyen. 2020. Adiponectin: Role in Physiology and Pathophysiology. *Int. J. Prev. Med.* *II*, 136.

1.1.2. Limitation of APN as an agonist and mimetic peptides

As previously described in part 1.1.2, APN regulates glucose and lipid metabolism by activating AdipoRs. Therefore, activating AdipoRs exerts protective effects on various pathologic conditions, including diabetes, obesity, cardiovascular disease, cancer, central nervous system disorders, and alopecia or chronic inflammatory skin diseases (Matsushita et al, 2006; Moon et al, 2013; Kim et al, 2015). Despite these various *in vitro* and *in vivo* experiments, it is difficult to convert APN into a practical drug form by several reasons: 1) limited delivery route considering the high molecular weight of APN, 2) unpredictable biological action caused by the fact that different oligomers of APN have varied biological properties and probably target different tissues *in vivo*, and 3) high production cost. To overcome these limitations, many researchers has been dedicated in developing small molecule-based or peptide-based agonists for AdipoRs, with screening molecular libraries, selecting possible sequences of APN globular domains, or using *in silico* model (Okada-Iwabu et al, 2013; Wang et al, 2017; Messaggio et al, 2017; Nicolas et al, 2018; Otvos et al, 2011; Otvos et al, 2014; Ma et al, 2017; Kim et al, 2018; Singh et al 2014). As of today, a summary of the reported small molecules and peptides can be found in **Table 1.1**.

Table 1 Published small molecules and mimetic peptides activating AdipoRs

Molecule	Sequence	In vitro activity	In vivo activity
AdipoRon (Small molecule)	-	- The EC50 value for AMPK activation is ~ 10 μ M - AdipoRon increases phosphorylated AMPK and ACC levels, and decreases the expression of adipogenic transcription factors C/EBP β , C/EBP α , and PPAR	- In an orthotopic pancreatic cancer model, AdipoRon at 5 mg/kg/day (administration mode not disclosed) for 14-days reduces tumor size and tumor area per tumor section by 50–75%. Administered intraperitoneally at 1 mg/kg/day for 21-days to mice, AdipoRon reverses corticosterone-induced depression-like state.
ADP355	<i>Asn-Ile-Pro-Nva-Leu-Tyr-Ser-Phe-Ala-Ser</i>	- Cancer cell growth inhibition (100nM) - Renal fibroblast differentiation inhibition	- Upon intraperitoneal injection into scid mice xenotransplanted with MCF-7 breast cancer tumor, ADP355 therapy at a 1 mg/kg/day dose decreases tumor size by 31% compared to untreated animals.
ADP399	<i>Asn-Ile-Pro-Nva-Leu-Tyr-Ser-Phe-Ala-Ser-His-Pro</i> ^a Dab- <i>Asn-Ile-Pro</i> ^b Nva-Leu-Tyr-Ser-Phe-Ala-Ser-His-Pro	- A 10-fold decrease of K562 chronic myeloid leukemia cell proliferation rate compared to monomeric ADP355, although this improvement is not obvious in animal models.	-
Pep70	Pro-Gly-Leu-Tyr-Tyr-Phe-Asp	- HSC-T6 cell proliferation inhibition with an IC50 of 5 μ M	-
BHD1028	Tyr-Tyr-Phe-Ala-Tyr-His-Pro-Asn-Ile-Pro-Gly-Leu-Tyr-Tyr-Phe	- Induction of AMPK phosphorylation in differentiated C2C12 myotubes (800nM)	-
GTDF (Non-peptidic agonist)	-	- Enhanced of glucose uptake and fatty acid oxidation	- Improvement of metabolic health (elevation of glucose clearance, β -cell survival, reduced steatohepatitis, browned white adipose tissue, and improvement of lipid profile) in an AdipoR1-expressing but not an AdipoR1-depleted strain of diabetic mice. The dose of GTDF in this instance was 10 mg/kg/day orally for 30 days.

^aDab is 2,4-diamino butyric acid, ^bL-Nva is norvaline, D-amino acids are printed in italics.

1.1.3. AdipoR1-related disease: Hair loss

Hair loss is an obvious distressing disorder affecting millions of people worldwide (Adil & Godwin, 2017). It is caused by various reasons including aging, hormonal dysfunction, and side effect of several medications (Price, 1999). Each mammalian hair follicle (HF) consists of cyclic phases of telogen (quiescence), anagen (regeneration), and catagen (degeneration) (Müller-Röver et al, 2001); thus, molecules that regulate the hair cycle to prolong or induce anagen phase by activating HF cells can be utilized as therapeutic agents (Ohn et al, 2019).

To date, two representative FDA-approved drugs, finasteride and minoxidil, are used to treat patients with patterned alopecia by regulating the HF cycle with promoting hair growth. Finasteride inhibits type II 5 α -reductase, suppressing the conversion of testosterone to dihydrotestosterone in HFs (Rittmaster, 1994). Minoxidil is used in topical form, although its exact underlying mode of action in treating alopecia needs to be elucidated (Messenger & Rundegren, 2004). Given their limited usage due to concerns of side effects or partial efficacy, new drugs with novel mechanisms of action to treat alopecia are highly demanded (Lucky et al, 2004; Gupta & Charrette, 2015).

The previous studies found that APN promotes hair growth *ex vivo* effectively, along with inducing mRNA expressions of key hair growth factors, including insulin-like growth factor 1 (IGF-1), vascular endothelial growth factor (VEGF), and hepatocyte growth factor (HGF), which suggests that

APN is a promising molecule to treat alopecia (Won et al, 2012). However, it is not well understood about the underlying action mechanism of APN on hair growth promotion and how to utilize this endogenous protein as clinically applicable drug forms (Otvos, 2019).

1.2. Materials and methods

1.2.1. Protein sequence database, MSA, conserved score calculation, and structure visualization

The amino acid sequence data of APN (372 amino acid sequences from 132 species) and AdipoR1 (213 amino acid sequences from 177 species) were obtained from UniProtKB through the website <https://www.uniprot.org/>. MSA of the protein sequences was created using Clustal Omega. The sequence logos were illustrated using Ggseqlogo. The degree of conservation of the physicochemical properties was calculated based on the previous literature (Livingstone & Barton, 1993), with background colored by conservation degree according to conditional formatting percentile rank among APN globular domain or AdipoR1 sequences. All structures of APN and AdipoR1 were visualized using PyMOL (PyMOL Molecular Graphics System, <https://pymol.org/>).

1.2.2. 3-(4,5-dimethylthiazol-2-yl)-2,5-diphenyltetrazolium bromide (MTT assay)

Dermal papilla cells and ORS cells were seeded into a 96-well plate (1.0×10^4 cells/well) with serum-free culture media for 24 h and then treated with each candidate 5-mer peptide (in 0.5 $\mu\text{g/ml}$ or 5 $\mu\text{g/ml}$) for 48 h. After the addition of MTT solution (20 μl , 5 mg/ml) to each well, the cells were

incubated for 4 h at 37°C in the dark room and then incubated with dimethyl sulfoxide (DMSO, 200 µl) for 20 min at room temperature. The samples were assessed by measuring the absorbance at 570 nm with an absorbance microplate reader (VersaMax).

1.2.3. Expression and purification of GST-fused pentapeptide

GST-fused P5 and P10 (**Figure 1.3A**) were expressed in *Escherichia coli* strain BL21 (DE3) cells induced with 0.5 mM isopropyl-β-D-1-thiogalactopyranoside (IPTG). Cells were lysed with a microfluidizer and the lysed cells were centrifuged at 4600 × g for 30 min at 277 K to pellet the cell debris; the supernatant was then applied to a glutathione-Sepharose column (GE Healthcare) pre-equilibrated with lysis buffer (20 mM Tris-HCl pH 8.0, 200 mM NaCl). Proteins were eluted with lysis buffer containing 15 mM reduced glutathione (**Figure 1.4**).

1.2.4. Pulldown assay

For analysis of the interaction of P5 to AdipoR1, the cDNAs encoding full-length AdipoR1 (residues 1–375) and N-terminal-truncated AdipoR1 (residues 89–375) were cloned into the p3×Flag_CMV vector (**Figure 1.3B**). Transfected HEK293T cells were lysed in lysis buffer (20 mM Tris-HCl pH 8.0, 200 mM NaCl, 1% Triton X-100, 1 mM PMSF, 4 µg/ml aprotinin, 10 µg/ml leupeptin, and 1 µg/ml pepstatin). For the interaction analysis, individually purified GST-fused P5 or P10 was incubated with glutathione–

Sepharose beads (20 μ l), AdipoR1-overexpressing cells were added to the beads, and the mixtures were gently rotated at 4°C overnight. After the beads were washed three times with phosphate-buffered saline containing Tween-20 (PBST) buffer (10 mM Na₂HPO₄, 1.8 mM KH₂PO₄, 2.7 mM KCl, 137mM NaCl, 0.05% v/v Tween-20 pH 7.4), the bound protein was eluted with 20 μ l of PBST buffer supplemented with glutathione (20 mM). Input and eluate samples were separated by SDS–PAGE, analyzed by Western blot using specific antibodies; DYKDDDDK tag mouse mAb (#8146, 1:1,000; Cell Signaling) and GST mouse mAb (#2624, 1:1,000; Cell Signaling) as primary antibody. Anti-mouse IgG HRP-linked antibody (#7076, 1:5,000; Cell Signaling) was used for secondary antibody. The membranes were visualized with enhanced chemiluminescent detection (#34580; Thermo Fisher). All constructs used in pulldown experiments were made by site-directed mutagenesis (**Table 1.2**).

1.2.5. Molecular docking of P5 to AdipoR1

We used GalaxyTongDock for docking the P5 to AdipoR1 (Ko et al, 2012; Park et al, 2019). GalaxyTongDock performs an exhaustive sampling of docking poses treating both protein and peptide as rigid structures by a fast Fourier transformation with improved energy parameters. The rigid body docking approach was employed here, assuming that the binding mode of P5 to AdipoR1 is similar to that of APN to the same receptor. The starting structure of AdipoR1 was obtained from the Protein Data Bank (PDB ID:

3WXV) (Tanabe et al, 2015), with deletion of the flexible C-terminal region at 365–373. P5 structure was extracted from that of APN (PDB ID: 4DOU) (Min et al, 2012). The transmembrane and cytoplasmic regions of AdipoR1 were excluded using the block option of GalaxyTongDock. The predicted docking poses were then relaxed by GalaxyRefineComplex (Heo et al, 2016).

1.2.6. RNA interference for AdipoR1

All transfections were performed using Lipofectamine 2000 following the manufacturer's instructions (#11668019; Thermo Fisher). Human DP and ORS cells were cultured without antibiotics until reaching 50% confluency. AdipoR1 or scrambled siRNA (Bioneer) was used. The culture medium was changed 6 h after transfection, and the cells were incubated for another 24 h before subsequent analyses.

1.2.7. Mouse hair cycle modulation

For the hair cycle modulation experiment, Adipoq^{-/-} (stock #008195; JAX) (Ma et al, 2002), Adipor1^{-/-} (Yamauchi et al, 2007; Okada-Iwabu et al, 2013), or C57BL/6 (KOATECH) female mice was used (Müller-Röver et al, 2001). They were housed (up to four animals per cage; 23 ± 2°C, 8:00–20:00, 12 h/12 h light/dark cycle). Mice were fed a standard chow diet and provided food and water ad libitum. Mice were randomly allocated and shaved dorsally at 7.5 weeks of age. The mouse hair growth score (a value from 0 to 100 based on the skin pigmentation and hair shaft density) was monitored and

documented at designated days with the experimenters being blind to the conditions, following a previous study (Chai et al, 2019). A higher score corresponds to a transition from telogen to anagen. On day 35, we obtained dorsal cutaneous tissue for histological analysis: anagen induction scores (calculated using an assigned arbitrary score; telogen = 1, anagen I–VI = 2–7) (Müller-Röver et al, 2001).

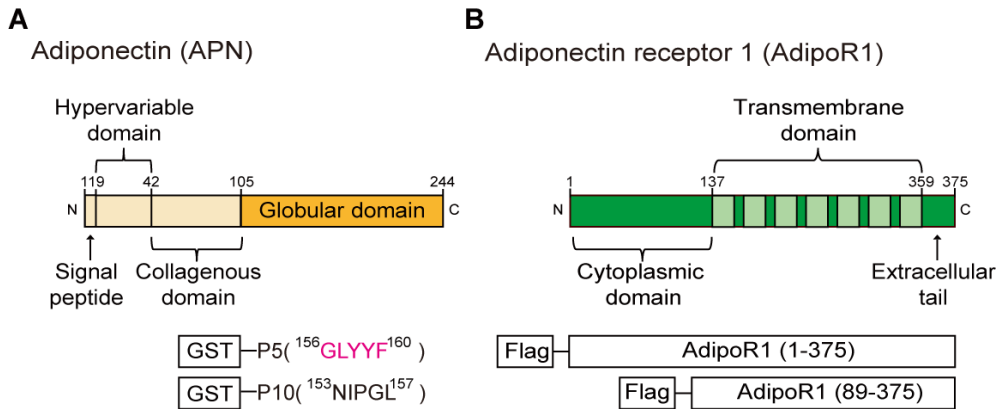


Figure 1.3 Construct design used in the experiment.

(A) Domain architectures of APN and the GST-fused 5-mer peptides (GLYYF; GST-P5, or NIPGL; GST-P10). (B) Domain architectures of AdipoR1 and Flag-fused full-length AdipoR1 (residue 1–375) or N-terminal-truncated AdipoR1 (residues 89–375). Each construct in the schematic diagram was used for the pulldown experiment.

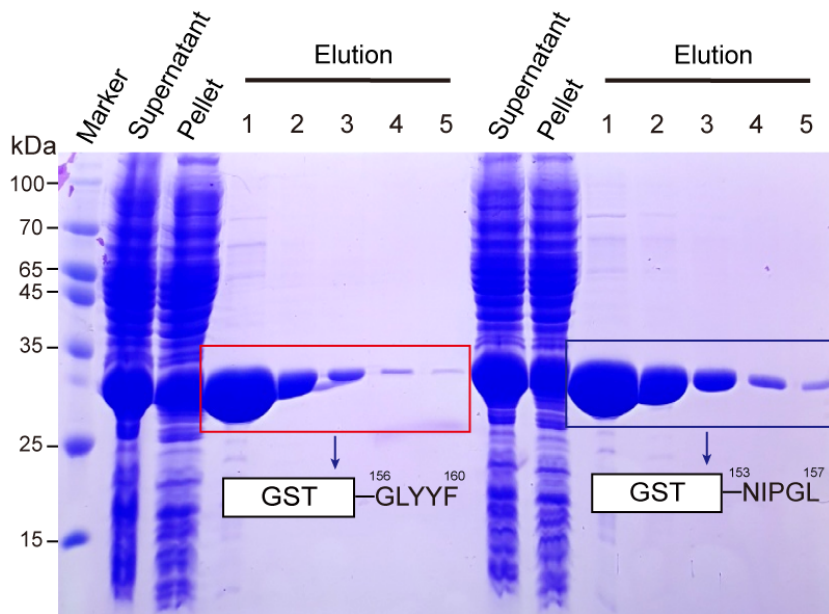


Figure 1.4 GST affinity purification of GST-fused pentapeptide.

GST-GLYYF and GST-NIPGL constructs were purified using the *E. coli* recombinant system. Lanes 1-5 are elution fractions of GST affinity chromatography. SDS-PAGE gels were visualized by using Coomassie blue.

Table 1.2 Primer sequences for site-directed mutagenesis

AdipoR1 (S231A)	
forward	TCTATTATTCCTTCTACTGCGCTCCACAGCCACG GCTCATCTA
reverse	TAGATGAGCCGTGGCTGTGGAGCGCAGTAGAAG GAATAATAGA
AdipoR1 (Y225A)	
Forward	GGAGCTTTGTCCCCTGGCTCGCTTATTCCTTCTA CTGCTCCCC
Reverse	GGGGAGCAGTAGAAGGAATAAGCGAGCCAGGG GACAAAGCTCC
AdipoR1 (Y226A)	
Forward	GCTTTGTCCCCTGGCTCTATGCTTCCTTCTACTGC TCCCCACA
Reverse	TGTGGGGAGCAGTAGAAGGAAGCATAGAGCCA GGGGACAAAGC
AdipoR1 (Y229A)	
Forward	CCTGGCTCTATTATTCCTTCGCTTGCTCCCCACA GCCACGGCT
Reverse	AGCCGTGGCTGTGGGGAGCAAGCGAAGGAATA ATAGAGCCAGG
AdipoR1 (F285A)	
Forward	GCGTCGTGCCACCACCATGCACGCTACTATCGCTGA GGGCTTTGT
Reverse	ACAAAGCCCTCAGCGATAGTAGCGTGCATGGTG GGCACGACGC
AdipoR1 (F285E)	
Forward	GCGTCGTGCCACCACCATGCACGAGACTATCGCTG AGGGCTTTGT
Reverse	ACAAAGCCCTCAGCGATAGTCTCGTGCATGGTG GGCACGACGC
AdipoR1 (F285Y)	
forward	GCGTCGTGCCACCACCATGCACTACACTATCGCTGA GGGCTTTGT
reverse	ACAAAGCCCTCAGCGATAGTGTAGTGCATGGTG GGCACGACGC
AdipoR1 (F285K)	
forward	GCGTCGTGCCACCACCATGCACAAGACTATCGCTG AGGGCTTTGT
reverse	ACAAAGCCCTCAGCGATAGTCTTGTGCATGGTG GGCACGACGC
AdipoR1 (E289A)	
forward	CCATGCACTTTACTATCGCTGCTGGCTTTGTCAA GGCCACCAC
reverse	GTGGTGGCCTTGACAAAGCCAGCAGCGATAGTA AAGTGCATGG
AdipoR1 (E289R)	
forward	CCATGCACTTTACTATCGCTCGCGGCTTTGTCAA GGCCACCAC

	GTGGTGGCCTTGACAAAGCC <u>GCG</u> AGCGATAGTA
reverse	AAGTGCATGG
AdipoR1 (F361A)	
	GAGTCTCCAACCTTCAGGAAG <u>CTC</u> GTTACGGCCT
forward	AGAAGGCGG
	CCGCCTTCTAGGCCGTAACG <u>AGCT</u> TTCCTGAAGGT
reverse	TGGAGACTC
AdipoR1 (R362A)	
	TCTCCAACCTTCAGGAATTC <u>GCT</u> TACGGCCTAGA
forward	AGGCGGCTG
	CAGCCGCCTTCTAGGCCGTA <u>AGC</u> GAATTCCTGA
reverse	AGGTTGGAGA
AdipoR1 (R362E)	
	TCTCCAACCTTCAGGAATTC <u>GAG</u> TACGGCCTAG
forward	AAGGCGGCTG
	CAGCCGCCTTCTAGGCCGTA <u>CTC</u> GAATTCCTGAA
reverse	GGTTGGAGA
AdipoR1 (E366A)	
	AGGAATTCCGTTACGGCCTAG <u>CTG</u> GCGGCTGTA
forward	CTGATGACAC
	GTGTCATCAGTACAGCCGCC <u>AGC</u> TAGGCCGTAA
reverse	CGGAATTCCT
AdipoR1 (F285A/E289A)	
	GCGTCGTGCCCACCATGCAC <u>GCT</u> ACTATCGCT <u>G</u> C
forward	<u>T</u> GGCTTTGT
	ACAAAGCC <u>AGC</u> AGCGATAGT <u>AGC</u> GTGCATGGTG
reverse	GGCACGACGC
AdipoR1 (F285E/E289A)	
	GCGTCGTGCCCACCATGCAC <u>GAG</u> ACTATCGCT <u>G</u> C
forward	<u>C</u> TGGCTTTGT
	ACAAAGCC <u>AGC</u> AGCGATAGT <u>CTC</u> GTGCATGGTG
reverse	GGCACGACGC

1.3. Results

1.3.1. Two potential small 5-mer peptides are positioned within a highly conserved sequence of APN

Human APN consists of four structural domains: a N-terminal signal peptide, a hypervariable domain, a collagenous domain, and a C-terminal globular domain, with the globular domain being biologically active (Fruebis et al, 2001; Tomas et al, 2002; Wong et al, 2004; Min et al, 2012). As an evolutionally conserved protein, APN shows a high degree of sequence homology in species with similar biological effects (Berg et al, 2002; Straub & Scherer, 2019). I identified the most conserved amino acid sequence of globular domain of APN using sequences from the UniProtKB database. I observed several highly conserved residues in APN, including Phe150, Gly156, and Tyr158, based on the degree of conservation of the physicochemical properties (**Figure 1.5**). Around the three most conserved amino acid residues (Phe150, Gly156, and Tyr158), a relatively highly conserved peptide sequence (148 GKFHCNIPGLYYFAY 162) was identified. This 15-mer sequence partially overlapped with or encompassed the sequence of AdipoRs agonists in previous studies (Otvos et al, 2011, 2014; Ma et al, 2017; Kim et al, 2018; Otvos, 2019).

To design transdermally deliverable AdipoR1 agonist, I further assessed the 15-mer sequence by cutting it into several 5-mer peptides (**Figure 1.6A**)

(Bos & Meinardi, 2000). Based on the fact that AdipoRs are expressed in HF cells, including dermal papilla (DP) and outer root sheath (ORS) cells (Won et al, 2012), we performed a cell proliferation assay on human DP and ORS cells to see if there is any potential biological effect of the 5-mer peptides on the human HF cells. Among the 5-mer peptides, 156GLYYF160 (P5) and 153NIPGL157 (P10) showed significant cell proliferative effects, providing a rationale to be assessed further (**Figure 1.6B**).

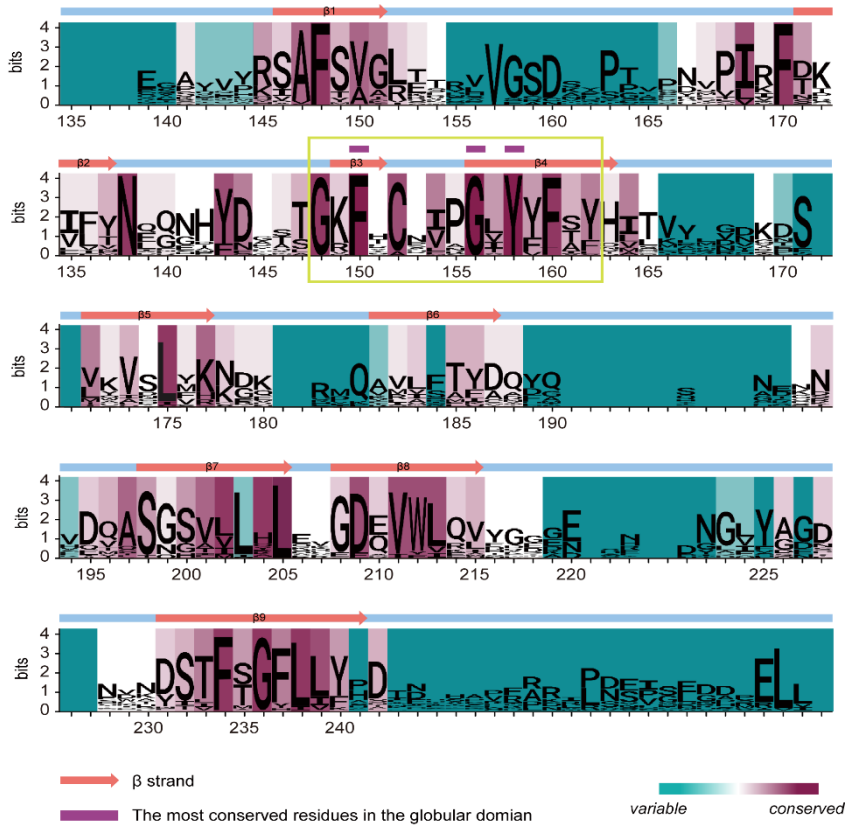


Figure 1.5 Excavation of the most conserved residues in APN globular domain.

Sequence logo landscape of MSA of APN globular domain. The residue numbers are based on the human APN amino acid sequence. In a given residue, the height of each letter (measured in bits) is proportionally scaled to the amount of information contributed based on Shannon entropy. The background color of each residue is determined by the degree of conservation of physicochemical properties (cyan to magenta). The most conserved residues (marked with purple tags) are located within a highly conserved sequence (designated in a green box).

A

APN 5-mer peptides	Peptide sequence
P3	G-K-F-H-C-N-I-P-G-L-Y-Y-F-A-Y
P4	G-K-F-H-C-N-I-P-G-L-Y-Y-F-A-Y
P5	G-K-F-H-C-N-I-P-G-L-Y-Y-F-A-Y
P6	G-K-F-H-C-N-I-P-G-L-Y-Y-F-A-Y
P7	G-K-F-H-C-N-I-P-G-L-Y-Y-F-A-Y
P8	G-K-F-H-C-N-I-P-G-L-Y-Y-F-A-Y
P9	G-K-F-H-C-N-I-P-G-L-Y-Y-F-A-Y
P10	G-K-F-H-C-N-I-P-G-L-Y-Y-F-A-Y

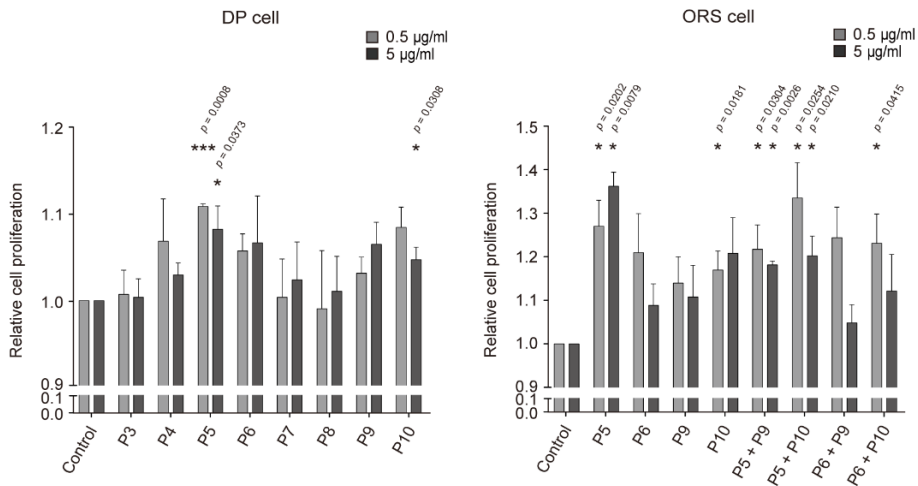
B

Figure 1.6 The screening of candidate 5-mer peptides based on DP and ORS cell proliferation.

(A) Candidate 5-mer peptide sequences derived from a highly conserved sequence of APN globular domain. Each sequence is indicated in black. (B)^① DP and ORS cells are used to screen the candidate 5-mer peptides in terms of the cell proliferation effect (n = 3–5 biological replicates/group)

^① Cell proliferation experiment was performed by Jungyoon Ohn, Ph.D. in Seoul National University

1.3.2. P5 directly binds with AdipoR1.

To investigate whether two potential 5-mer peptides (P5 and P10) directly bind to AdipoR1, I performed protein-protein interaction assays using glutathione S-transferase (GST) pulldown method. After the purified GST-fused P5 or P10 peptides were immobilized to GST beads, they were mixed with human embryonic kidney (HEK) 293T cell lysate expressing full-length AdipoR1 (residues 1–375), and the pulldown fractions were analyzed by Western blots using Flag and GST antibodies, respectively. Surprisingly, we found that only P5 bound to AdipoR1 whereas P10 did not (**Figure 1.7**). Similar to G protein-coupled receptors, AdipoRs consist of seven transmembrane helices; however, they oriented oppositely to G protein-coupled receptors in that the N-terminal is located in the cytoplasm, while the C-terminal is located in the extracellular space (Tanabe et al, 2015; Vasiliauskaitė-Brooks et al, 2017). Therefore, I also checked whether P5 could bind to an N-terminal-truncated AdipoR1 (residues 89–375), assuming that the N-terminal part of AdipoR1 does not contribute to the AdipoR1-P5 complex formation. As expected, both full-length and N-terminal-truncated AdipoR1 (residues 1–375 and 89–375, respectively) bound to P5 (**Figure 1.8**). For further analysis of the molecular interaction between AdipoR1 and P5 in viable cells, P5 conjugated with fluorescein isothiocyanate (FiTC-P5, **Figure 1.9A**) was treated on human ORS cells *in vitro*. Indeed, FiTC-P5 was colocalized with AdipoR1 (**Figure 1.9B**), suggesting that the molecular interaction between AdipoR1 and P5 is also present in viable cells *in vitro*.

When I examined the position of P5 in APN structure (PDB ID: 4DOU) (Min et al, 2012), P5 is a part of the β sheets in the jelly roll fold, which are arranged in two 5-strand layers (**Figure 1.10**). I hypothesized that the side chains of P5, which potentially bind to AdipoR1, will be surface-exposed in APN structure if P5 moiety is hotspot of APN for binding to AdipoR1. Indeed, the second and fourth residues of P5 (Leu and Tyr, respectively) are surface-exposed. Meanwhile, the third and fifth residues (Tyr and Phe, respectively) form a core interaction within APN, suggesting that they are crucial to maintain the correct folding of APN (**Figure 1.10**).

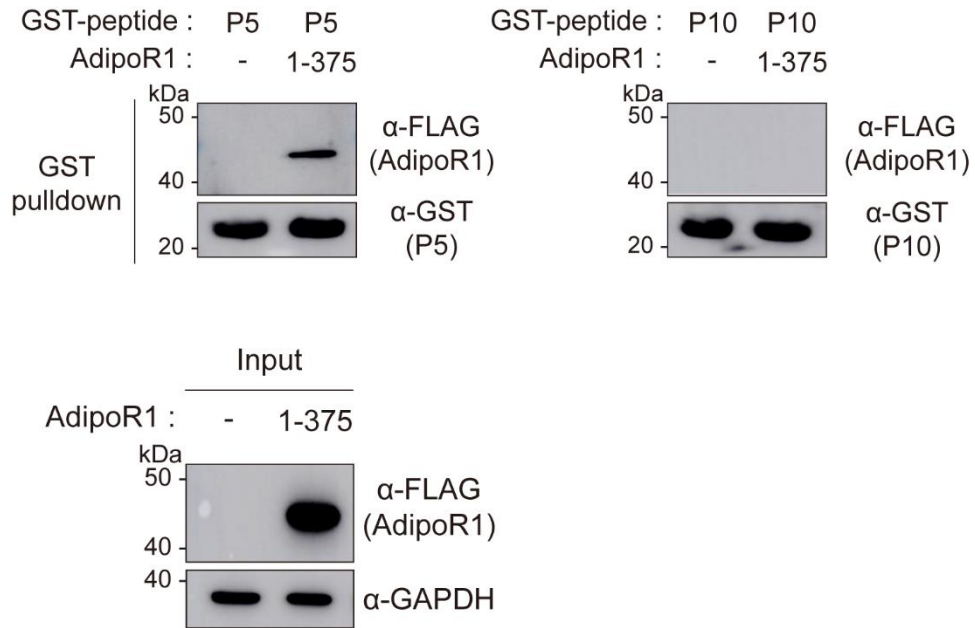


Figure 1.7 Direct molecular interaction between the P5 and AdipoR1

GST pull-down of transiently expressed AdipoR1 (residues 1–375) with immobilized GST-P5 or GST-P10 fusion proteins. Pull-down fractions were subjected to western blotting using Flag and GST antibodies.

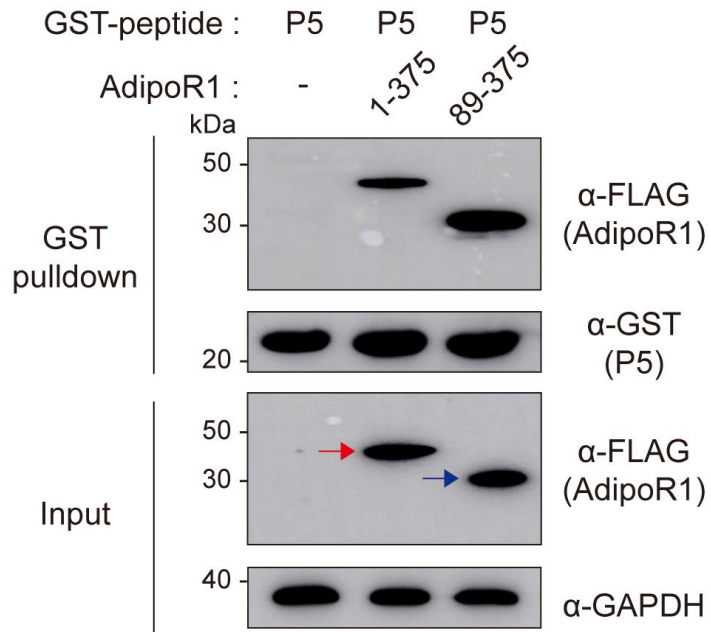
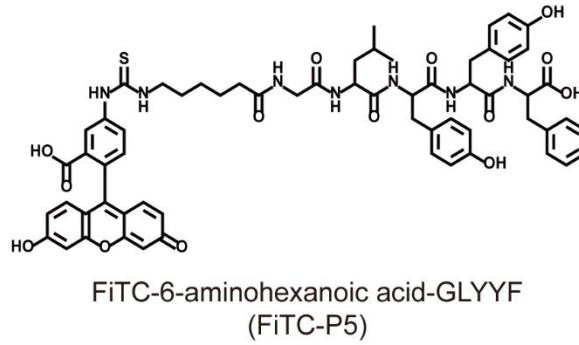


Figure 1.8 P5 binds to both full-length AdipoR1 and N-terminal-truncated AdipoR1.

GST pulldown of AdipoR1 (residues 1–375) or AdipoR1 (residues 89–375) with GST-P5. The red or blue arrow indicates correct sized bands of AdipoR1 (residues 1–375) or AdipoR1 (residues 89–375), respectively.

A



B

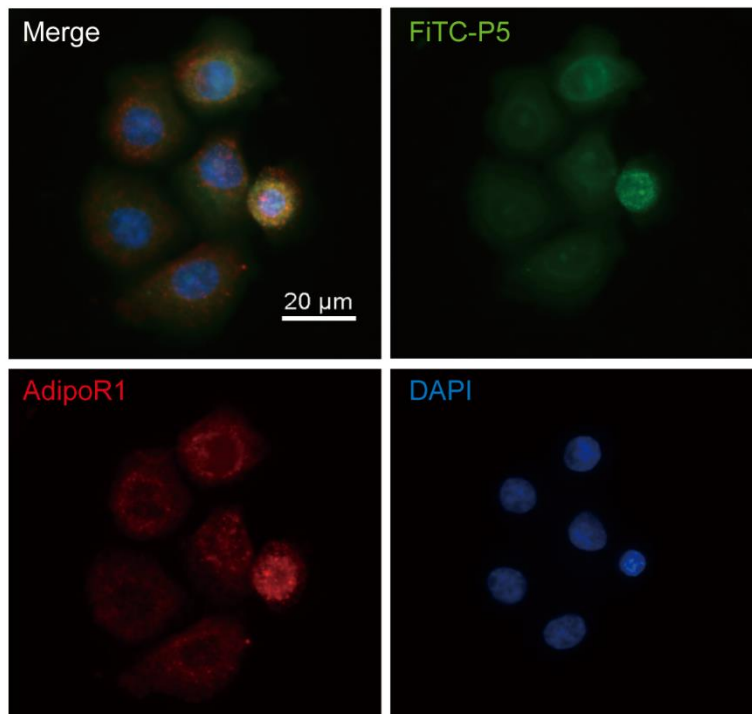


Figure 1.9 ^②The colocalization of P5 and AdipoR1 *in vitro*.

(A) Molecular structure of the FITC-conjugated P5 (FITC-P5). (B) IF staining for AdipoR1 and FITC-P5 in cultured FITC-P5-treated ORS cells

^② IF staining experiment was performed by Jungyoon Ohn, Ph.D. in Seoul National University

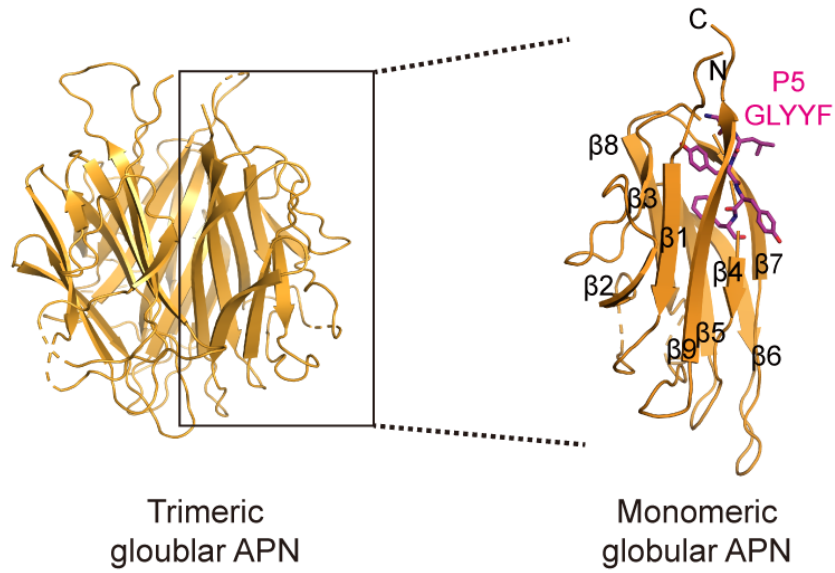


Figure 1.10 The position of P5 in APN.

Overall structure of trimeric globular APN in ribbon cartoon representation (PDB ID: 4DOU). A ribbon diagram of monomeric globular APN is drawn, and P5 is shown in magenta sticks.

1.3.3. Structural analysis of the specific binding pocket of AdipoR1 for P5

To investigate how P5 binds to AdipoR1 at the atomic level, the protein-peptide docking simulation using the GalaxyTongDock (Ko et al, 2012; Park et al, 2019) was performed. To predict the structure of AdipoR1-P5 complex, the available human AdipoR1 crystal structure (residues 89–364, PDB ID: 3WXV) (Tanabe et al, 2015) was used as a starting model. Several models that meet the following three conditions were generated and closely examined: first, both the N- and C-termini of P5 are not buried because P5 is located in the middle of APN; second, the fourth residue Tyr forms a hydrophobic interaction with AdipoR1 because the fourth position is well conserved with aromatic residues; third, the highly conserved residues on the extracellular region of AdipoR1 participate in the binding.

Finally, an optimal docking model for the AdipoR1-P5 complex was selected, in which the protruding side chain of the fourth residue Tyr in P5 is docked to the inner hydrophobic pocket of AdipoR1, forming strong hydrophobic interactions with Tyr225 and Tyr226 in extracellular loop 2 of AdipoR1 protein (**Figure 1.11A and B**). Interestingly, these two residues in extracellular loop 2 of AdipoR1 were relatively conserved along with Tyr229, based on the multiple sequence alignment (MSA) results using AdipoR1 sequences (**Figure 1.12**). Both the N- and C-termini of P5 are surface-exposed (**Figure 1.11A**); thus, APN forms a complex with AdipoR1 without any significant steric clash when the structure of APN was docked in that of

the AdipoR1-P5 complex by superimposing P5. These data confirmed that our AdipoR1-P5 complex docking model is reasonable (**Figure 1.13**).

To validate this model, I mutated three residues (Tyr225, Tyr226, and Tyr229) of AdipoR1 and assessed their interactions with P5 by GST pulldown assays. As expected, mutations of the two interfacial residues (Y225A and Y226A) resulted in significant reductions of the pulldown efficiency compared to WT, while Y229A mutation showed no reduction (**Figure 1.14A**). These results suggest that the hydrophobic pocket of AdipoR1 consisting of Tyr225 and Tyr226 might be important for binding to P5. To examine contributions of other surface-exposed residues on the extracellular surface of AdipoR1, I generated single or double mutants (F285A, F285E, F361A, R362A, F285E/E289A, F285E/F361A, or F285A/R362A) of AdipoR1 and evaluated their interactions with P5 (**Figure 1.14B and C**). Notably, mutations of Phe285 to Ala or Glu significantly reduced the pulldown efficiency, and double mutants of AdipoR1 containing the Phe285 mutation (F285E/E289A, F285E/F361A, or F285A/R362A) also showed significantly reduced pulldown efficiency, implying that Phe285 plays a crucial role in P5 binding (**Figure 1.14B and C**). In addition, other two mutants (F361A and R362A) showed mild reduction in their pulldown efficiency for P5 (**Figure 1.14B**). However, each pulldown efficiency of P5 for AdipoR1 with the other single mutants (F285Y, F285K, E289R, or E366R) or double mutants (F285A/F361A) was not decreased (**Figure 1.15**). For further confirmation of this model, two purified GST-fused peptides (GLYDF

and GLYAF; the fourth Tyr of P5 was mutated into Asp or Ala, respectively) were purified and evaluated for their pulldown efficiency for AdipoR1. As expected, the two GST-fused peptides showed significantly lower pulldown efficiency for AdipoR1 than P5 (**Figure 1.16**). Taken together, these intensive mutational studies for interfacial residues of AdipoR1 and P5 amply support our docking model.

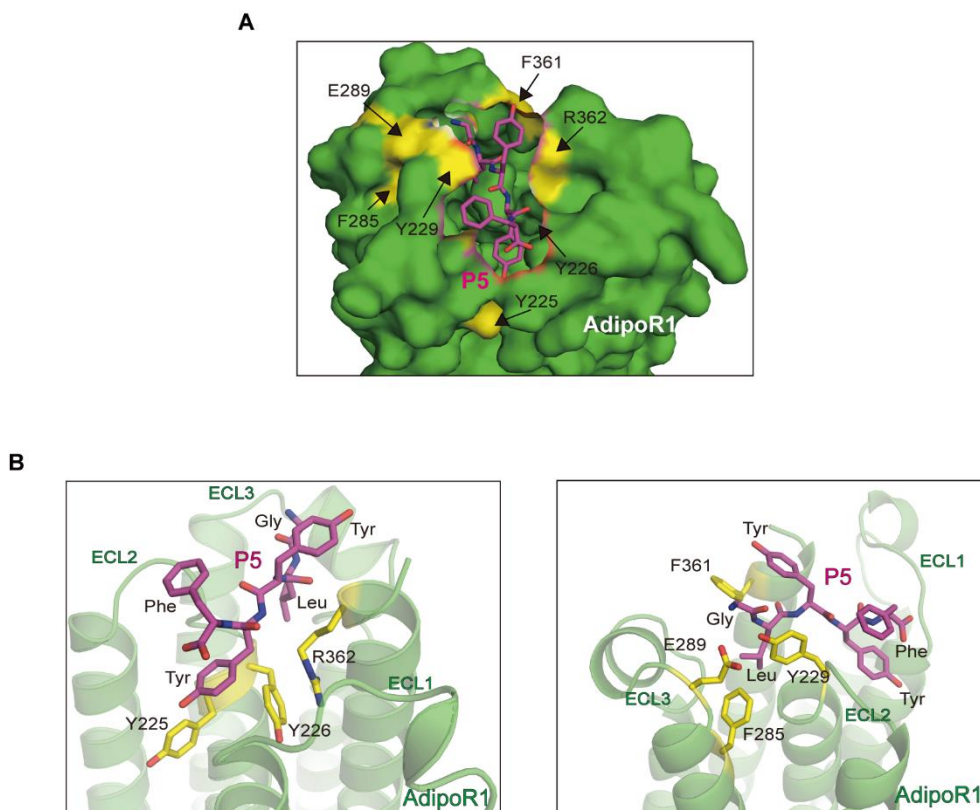


Figure 1.11^③ The most optimal docking model for the AdipoR1-P5 complex

(A) P5 is shown in magenta sticks. Each amino acid of AdipoR1 in yellow was mutated in the following experiments. (B) The magnified view for the detailed AdipoR1-P5 complex interface (magenta, P5; yellow, amino acids of AdipoR1); ECL, extracellular loop of AdipoR1.

^③ Molecular docking simulation was performed by Taeyong Park, Ph.D. in Seoul National University

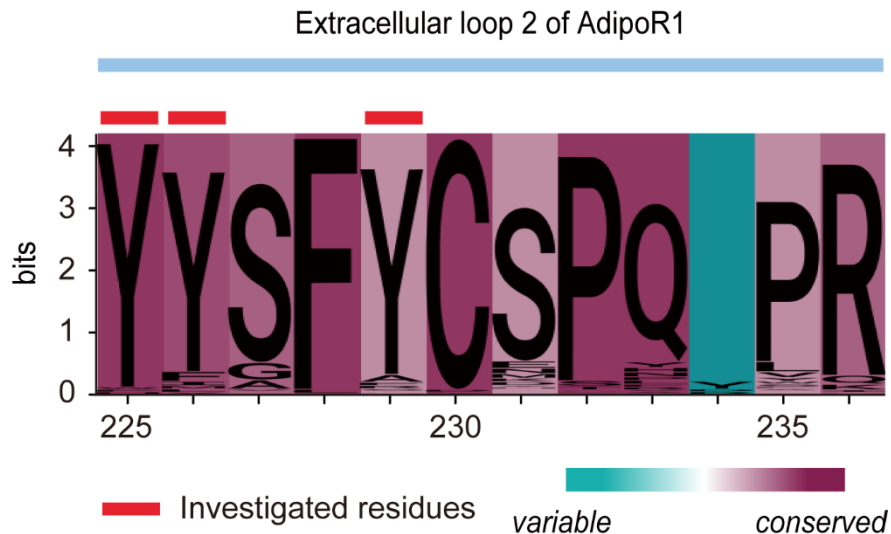


Figure 1.12 Sequence logo landscape of MSA of extracellular loop 2 of AdipoR1.

The residue numbers are based on the human AdipoR1 amino acid sequence. In a given residue, the height of each letter (measured in bits) is proportionally scaled to the amount of information contributed based on Shannon entropy. The background color of each residue is determined by the degree of conservation in physicochemical properties (cyan to magenta). The investigated residues in the text are marked with red tags (Tyr225, Tyr226, and Tyr229).

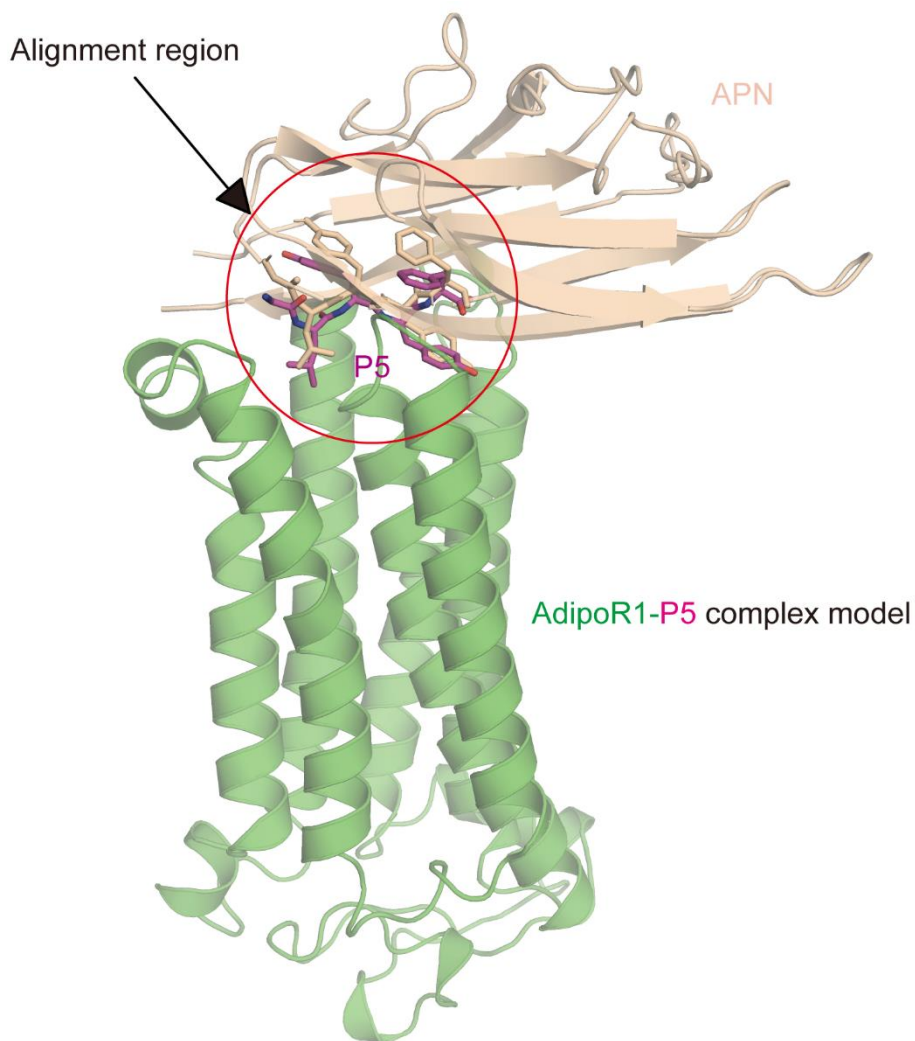


Figure 1.13 Cartoon diagram of the superposition of APN with the docking model of the AdipoR1-P5 complex.

The red circle indicates the position of P5. AdipoR1 (PDB ID: 3WXV), APN (PDB ID: 4DOU), and P5 are colored green, wheat, and magenta, respectively.

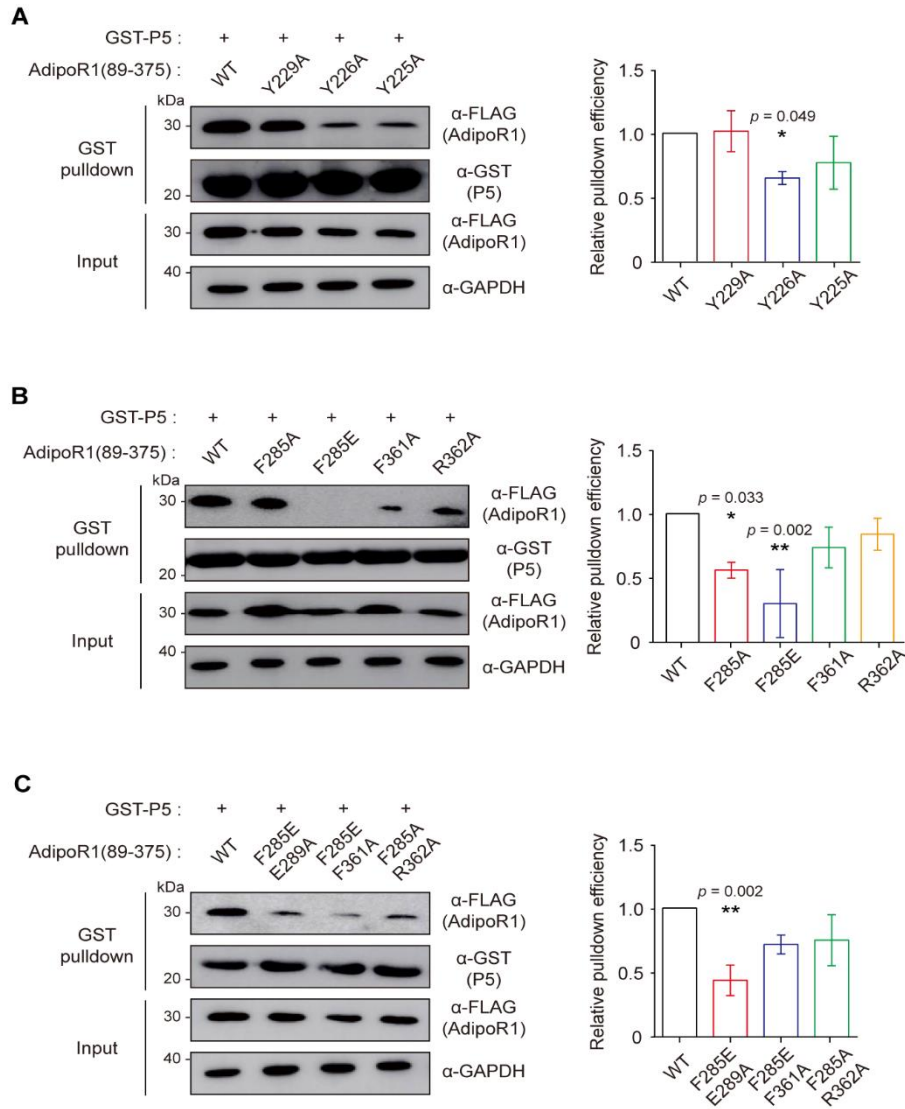


Figure 1.14 Mutational studies based on molecular docking simulation.

(A)-(C) Pulldown of Flag-fused AdipoR1 input (residues 89–375) with amino acid mutation(s), as indicated, with GST-P5. The relative pulldown efficiency is expressed as the ratio of the band intensities of bound AdipoR1 to those of AdipoR1 (residue 89–375) inputs, as indicated (n = 3 technical replicates/group).

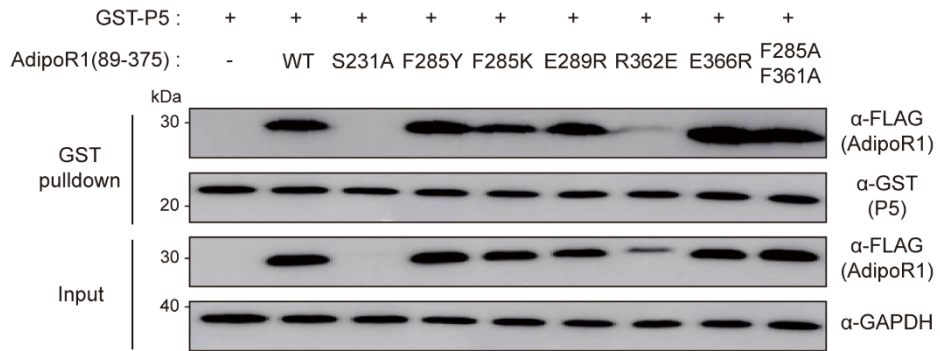


Figure 1.15 Pulldown of AdipoR1 mutants (residues 89–375) with the GST-fused P5

GST pulldown of P5 for AdipoR1 with the other single mutants (S213A, F285Y, F285K, E289R, R362E, or E366R) or double mutants (F285A/F361A). AdipoR1 was not expressed in S213A and R362E, and there were no significant changes compared to WT for the remaining other mutants.

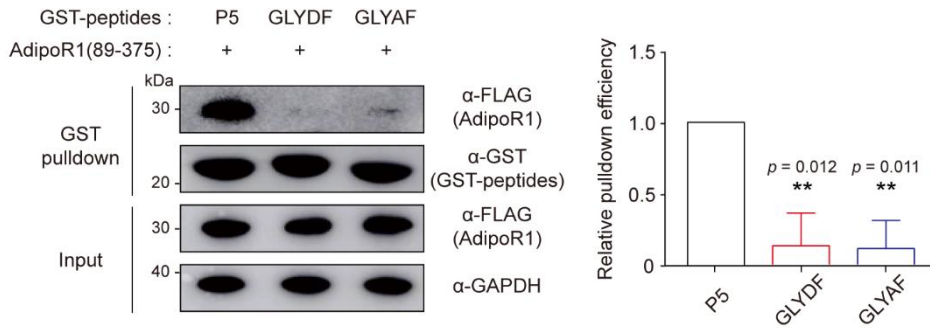


Figure 1.16 Pulldown of AdipoR1 (residues 89–375) with GST-P5 or GST-fused to two mutant peptides (GLYDF and GLYAF).

Two GST-fused mutant peptides (GLYDF and GLYAF; the fourth Tyr of P5 was mutated into Asp or Ala, respectively) evaluated for their pulldown efficiency for AdipoR1. The relative pulldown efficiency is expressed as the ratio of the band intensities of bound AdipoR1 to those of AdipoR1 (residue 89–375) inputs, as indicated (n = 3 technical replicates/group).

1.3.4. P5 activates AMPK signaling pathway through AdipoR1 in ORS and DP cells

Following the confirmation of the molecular interaction between AdipoR1 and P5, the activation of the intracellular signaling pathway by P5 was evaluated. APN treatment on ORS and DP cells could activate AMPK signaling pathways, which are previously known to be downstream effectors of AdipoR1 (Mao et al, 2006; Deepa & Dong, 2009; Shibata et al, 2012). Accordingly, whether P5 could also activate AMPK signaling pathway was investigated. Using P5 for treatment on ORS and DP cells, the concentration-dependent phosphorylation of AMPK was observed (**Figure 1.17A**). Next, whether both P5 the phosphorylation of AMPK through AdipoR1 in ORS and DP cells was examined. Based on western blot analysis after the AdipoR1 siRNA transfection, the p-AMPK intensity was reduced in both transfected ORS and DP cells after P5 or APN treatment (**Figure 1.17B**). Collectively, P5 activates AMPK signaling pathway through AdipoR1 in ORS and DP cells *in vitro*.

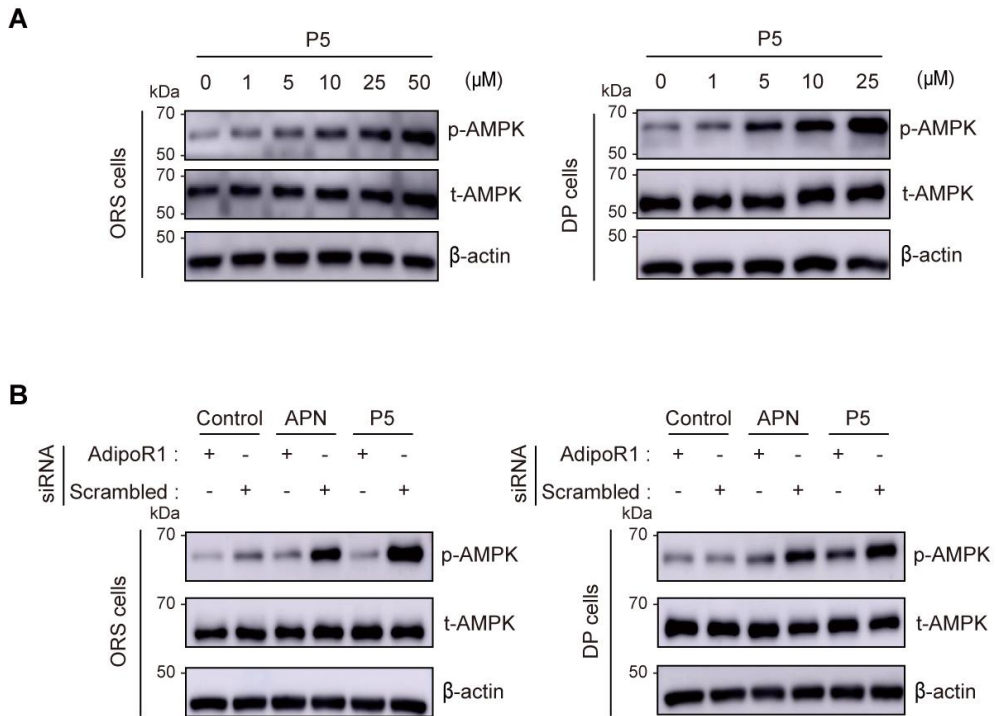


Figure 1.17 P5 activate AMPK signaling pathway through AdipoR1 *in vitro*.^④

(A) P5-treated ORS or DP cells lysates were analyzed for p-AMPK and t-AMPK. Densitometric analysis for the ratio of p-AMPK protein to t-AMPK protein (n = 5 (ORS) and 4 (DP) biological replicates/group). (B) AdipoR1 siRNA-transfected ORS or DP cells were treated with APN or P5. The cell lysates were analyzed for p-AMPK

^④ Western blot and RNA interference analysis were performed by Jungyoon Ohn, Ph.D. in Seoul National University

1.3.5. Topical P5 treatment induced the anagen hair cycle *in vivo*

Based on a series of molecular and biological studies, we confirmed that P5 interacts with AdipoR1 and activates AMPK signaling, likewise APN. We needed to check if this worked *in vivo*. Our previous studies found that APN promotes hair growth effectively, along with inducing mRNA expressions of key hair growth factors (Won et al, 2012). We tested whether P5 can accelerate hair growth *in vivo*, using hair cycle modulation assay in mice.

We evaluated P5 effect in Adipoq^{-/-} mouse (Ma et al, 2002). Skin pigmentation was prominent in P5-treated Adipoq^{-/-} mice at day 14 (**Figure 18A**). In contrast, no obvious pigmentation was observed in vehicle-treated Adipoq^{-/-} mice. At day 35, unlike vehicle-treated Adipoq^{-/-} mice showing little pigmentation, P5-treated Adipoq^{-/-} mice manifested hairs with pigmentation (**Figure 18A**). The hair cycle score was significantly different between P5- and vehicle-treated Adipoq^{-/-} mice. To test whether the effect of P5 is mediated through AdipoR1 *in vivo*, we used Adipor1^{-/-} mice (Yamauchi et al, 2007; Okada-Iwabu et al, 2013). Consistently, the anagen induction effects of P5 was abolished in the Adipor1^{-/-} mice (**Figure 1.18B**). Taken together, topical P5 treatment can accelerate hair growth through AdipoR1 *in vivo*.

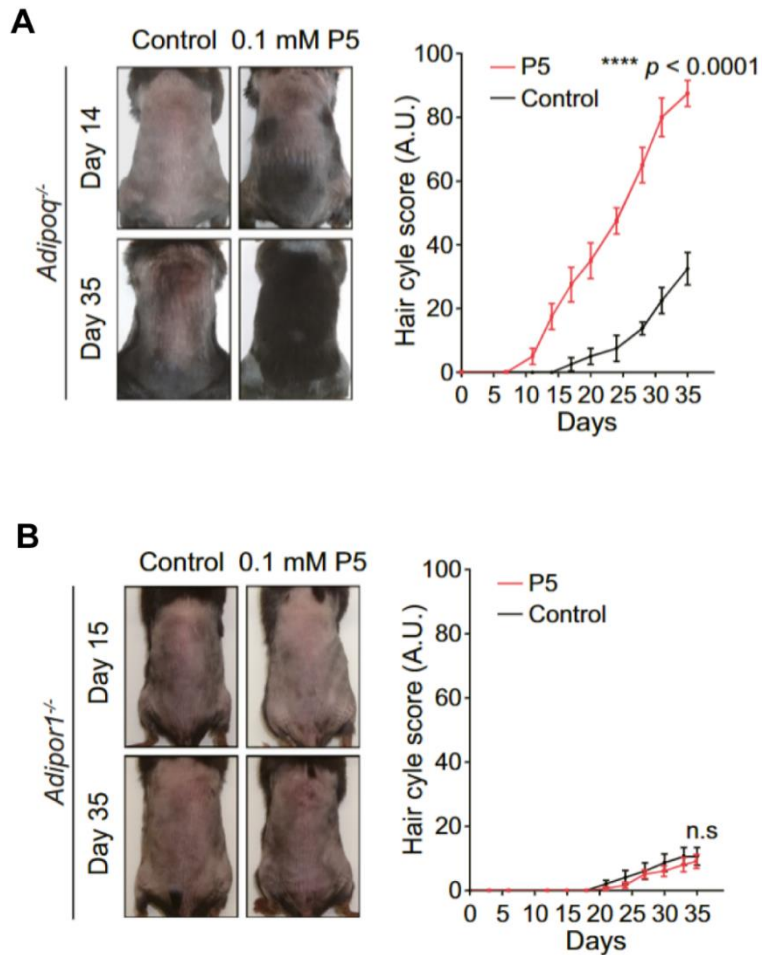


Figure 1.18 ^⑤Topical P5 treatment induced the anagen hair cycle through AdipoR1 *in vivo*.

(A) Gross morphology of vehicle-, or P5-treated Adipoq^{-/-} mice. Hair cycle scores of vehicle-, or P5-treated Adipoq^{-/-} mice (n = 4 mice/group); Two-way ANOVA. (B) Gross morphology of vehicle-, or P5-treated Adipor1^{-/-} mice. Hair cycle scores of vehicle-, or P5-treated Adipor1^{-/-} mice (n = 5 mice/group); Two-way ANOVA.

^⑤ Hair cycle modulation experiments were performed by Jungyoon Ohn, Ph.D. in Seoul National University

1.4. Discussion

APN, one of the most important and extensively investigated adipokines (Nakano et al, 1996; Pajvani et al, 2003), binds to the extracellular portion of AdipoR1, activates AMPK signaling pathway, and exerts protective effects on cells (Tomas et al, 2002; Kahn et al, 2005; Mao et al, 2006; Deepa & Dong, 2009; Straub & Scherer, 2019). Low systemic APN level is implicated as a risk factor for many human diseases, such as obesity, obesity-associated malignancies, metabolic syndrome, cardiovascular disease, and type II diabetes (Berg et al, 2002; Pischon et al, 2004; Li et al, 2009; Straub & Scherer, 2019). In chronic inflammatory skin conditions in humans, including psoriasis, photoaging, and sensitive skin syndrome, the APN level in cutaneous and subcutaneous fat tissue is decreased (Kim et al, 2015, 2016; Shibata et al, 2015). Taken together, exogenous APN for activating AdipoRs could be beneficial for several human diseases.

However, it is limited to use exogenous APN as an AdipoRs modulator in humans (Otvos, 2019). Instead, many researchers have developed peptide-based or small molecule-based AdipoRs activators (Otvos et al, 2011, 2014; Okada-Iwabu et al, 2013; Singh et al, 2014; Ma et al, 2017; Kim et al, 2018; Otvos, 2019). An octapeptide identified by screening a sequence-based library is able to activate AdipoRs (Otvos et al, 2011). To improve the stability and solubility, ADP355 consisting of non-natural residues has been developed (Otvos et al, 2014). Beside peptides, agonistic small molecules of AdipoRs,

such as AdipoRon and GTDF, have also been developed and investigated widely (Okada-Iwabu et al, 2013; Singh et al, 2014). However, it is not elucidated whether the agonists are effective in alleviating alopecia, especially via transdermal delivery route in a topical form. It is crucial that a therapeutic strategy for alopecia should affect only in the intended area locally to minimize unwanted systemic side effects.

In this study, it was confirmed that the transdermally deliverable P5 activates AMPK signaling pathway through AdipoR1 increasing hair growth factor expression in human DP *in vitro*. Furthermore, P5 treatment induced anagen hair cycle in *in vivo* mouse models, which is mediated by AMPK signaling pathway, a downstream effector of AdipoR1 (Mao et al, 2006; Deepa & Dong, 2009). Collectively, P5 is a promising drug candidate which is a topically applicable molecule for alleviating alopecia. In further, human clinical trials are necessary to utilize topical P5 application for the treatment of alopecia patients in the clinical setting.

Furthermore, I tried to obtain the AdipoR1-APN complex *in vitro*, but I could not observe the co-elution band of AdipoR1 and APN. This result was different from our expectation that the C-terminus of AdipoR1 would bind to the pocket that forms the trimer of APN. Nevertheless, this study is noteworthy in that the agonistic structure of APN binding to AdipoR1 is specified into pentapeptide, along with revealing the key spot of AdipoR1. The fact that the key spot of AdipoR1 for APN has been largely unknown hinders the development of effective drug molecules targeting AdipoR1.

Based on the docking studies followed by extensive mutational studies, the inner hydrophobic cleft of AdipoR1 consisting of Tyr225 and Tyr226 is suggested to be a crucial region for activating AdipoR1 upon the agonist binding. This newly identified key spot might be useful to further design AdipoR1 activating molecules for various biological beneficial consequences, given that upregulating AdipoR1 would result positive impacts on aforementioned human diseases.

In summary, we successively narrowed down the sequences of globular APN into the pentapeptide (GLYYF: P5), which can bind to and activate AdipoR1. The comprehensive molecular and biological evidences showed its efficacy on hair growth promotion through AdipoR1 signaling pathway after topical application. Moreover, the findings of the crucial region in AdipoR1 for binding to P5 pave the way for the development of novel AdipoR1 modulating molecules in the future.

1.5. Reference

- Adil A, Godwin M. (2017). The effectiveness of treatments for androgenetic alopecia: a systematic review and meta-analysis. *J Am Acad Dermatol.* **77**, 136-141.
- Berg AH, Combs TP, Scherer PE. (2002). ACRP30/adiponectin: an adipokine regulating glucose and lipid metabolism. *Trends Endocrinol Metab.* **13**, 84-89.
- Bos JD, Meinardi MM. (2000). The 500 Dalton rule for the skin penetration of chemical compounds and drugs. *Exp Dermatol.* **9**, 165-169.
- Chai M, Jiang M, Vergnes L, Fu X, de Barros SC, Doan NB, Huang W, Chu J, Jiao J, Herschman H, Crooks GM, Reue K, Huang J. (2019). Stimulation of hair growth by small molecules that activate autophagy. *Cell Rep.* **27**, 3413-3421.
- Deepa SS, Dong LQ. (2009). APPL1: role in adiponectin signaling and beyond. *Am J Physiol Endocrinol Metab.* **296**, E22-E36.
- Fruebis J, Tsao TS, Javorschi S, Ebbets-Reed D, Erickson MR, Yen FT, Bihain BE, Lodish HF. (2001). Proteolytic cleavage product of 30-kDa adipocyte complement-related protein increases fatty acid oxidation in muscle and causes weight loss in mice. *Proc Natl Acad Sci USA.* **298**, 2005-2010.

- Gupta AK, Charrette A. (2015). Topical minoxidil: systematic review and meta-analysis of its efficacy in androgenetic alopecia. *Skinmed*. **13**, 185-189.
- Heo L, Lee H, Seok C. (2016). GalaxyRefineComplex: refinement of protein-protein complex model structures driven by interface repacking. *Sci Rep*. **6**, 32153.
- Kahn BB, Alquier T, Carling D, Hardie DG. (2005). AMP-activated protein kinase: ancient energy gauge provides clues to modern understanding of metabolism. *Cell Metab*. **1**, 15-25.
- Kim EJ, Lee DH, Kim YK, Eun HC, Chung JH. (2015). Adiponectin Deficiency Contributes to Sensitivity in Human Skin. *The Journal of investigative dermatology*. **135**, 2331-2334.
- Kim S, Lee Y, Kim JW, Son YJ, Ma MJ, Um JH, Kim ND, Min SH, Kim DI, Kim BB. (2018). Discovery of a novel potent peptide agonist to adiponectin receptor 1. *PLoS ONE*. **13**, e0199256.
- Ko J, Park H, Heo L, Seok C. (2012). GalaxyWEB server for protein structure prediction and refinement. *Nucleic Acids Res*. **40**, W294-W297.
- Li S, Shin HJ, Ding EL, van Dam RM. (2009). Adiponectin levels and risk of type 2 diabetes: a systematic review and meta-analysis. *JAMA*. **302**, 179-188.
- Livingstone CD, Barton GJ. (1993). Protein sequence alignments: a strategy

for the hierarchical analysis of residue conservation. *Comput Appl Biosci.* **9**, 745-756.

Lucky AW, Piacquadio DJ, Ditre CM, Dunlap F, Kantor I, Pandya AG, Savin RC, Tharp MD. (2004). A randomized, placebo-controlled trial of 5% and 2% topical minoxidil solutions in the treatment of female pattern hair loss. *J Am Acad Dermatol.* **50**, 541-553.

Ma L, Zhang Z, Xue X, Wan Y, Ye B, Lin K. (2017). A potent peptide as adiponectin receptor 1 agonist to against fibrosis. *J Enzyme Inhib Med Chem.* **32**, 624-631.

Matsushita K, Yatsuya H, Tamakoshi K, Wada K, Otsuka R, Takefuji S, Sugiura K, Kondo T, Murohara T, Toyoshima H. (2006). Comparison of circulating adiponectin and proinflammatory markers regarding their association with metabolic syndrome in Japanese men. *Arterioscler Thromb Vasc Biol.* **26**, 871-876

Mao X, Kikani CK, Riojas RA, Langlais P, Wang L, Ramos FJ, Fang Q, Christ-Roberts CY, Hong JY, Kim RY, Liu F, Dong LQ. (2006). APPL1 binds to adiponectin receptors and mediates adiponectin signaling and function. *Nat Cell Biol.* **8**, 516-523.

Messaggio F, Mendonsa AM, Castellanos J, Nagathihalli NS, Gorden L, Merchant NB, VanSaun MN. (2017). Adiponectin receptor agonists inhibit leptin induced pSTAT3 and in vivo pancreatic tumor growth. *Oncotarget.*

8, 85378-85391.

Messenger AG, Rundegren J. (2004). Minoxidil: mechanisms of action on hair growth. *Br J Dermatol.* **150**, 186-194.

Min X, Lemon B, Tang J, Liu Q, Zhang R, Walker N, Li Y, Wang Z. (2012). Crystal structure of a single-chain trimer of human adiponectin globular domain. *FEBS Lett.* **586**, 912-917.

Moon HS & Mantzoros CS. (2013). Adiponectin and metformin additively attenuate IL1 β -induced malignant potential of colon cancer. *Endocr Relat Cancer.* **20**, 849-859.

Müller-Röver S, Foitzik K, Paus R, Handjiski B, van der Veen C, Eichmüller S, McKay IA, Stenn KS. (2001). A comprehensive guide for the accurate classification of murine hair follicles in distinct hair cycle stages. *J Invest Dermatol.* **117**, 3-15.

Nakano Y, Tobe T, Choi-Miura NH, Mazda T, Tomita M. (1996). Isolation and characterization of GBP28, a novel gelatin-binding protein purified from human plasma. *J Biochem.* **120**, 803-812.

Nicolas S, Debayle D, Béchade C, Maroteaux L, Gay AS, Bayer P, Heurteaux C, Guyon A, Chabry J. (2018). AdipoRon, an adiponectin receptor agonist acts as an antidepressant and metabolic regulator in a mouse model of depression. *Transl Psychiatry.* **8**, 159.

Ohn J, Kim KH, Kwon O. (2019). Evaluating hair growth promoting effects of candidate substance: a review of research methods. *J Dermatol Sci.* **93**, 144-149.

Okada-Iwabu M, Yamauchi T, Iwabu M, Honma T, Hamagami KI, Matsuda K, Yamaguchi M, Tanebe H, Kimura-Someya T, Shirouzu M, Ogata H, Tokuyama K, Ueki K, Nagano T, Tanaka A, Yokoyama S, Kadowaki T. (2013). A small-molecule AdipoR agonist for type 2 diabetes and short life in obesity. *Nature.* **503**, 493-499.

Otvos L Jr, Haspinger E, La Russa F, Maspero F, Graziano P, Kovalszky I, Lovas S, Nama K, Hoffman R, Knappe D, Cassone M, Wade J, Surmacz E. (2011). Design and development of a peptide-based adiponectin receptor agonist for cancer treatment. *BMC Biotechnol.* **11**, 90.

Otvos L Jr, Knappe D, Hoffmann R, Kovalszky I, Olah J, Hewitson TD, Stawikowska R, Stawikowski M, Cudic P, Lin F, Wade JD, Surmacz E, Lovas S. (2014). Development of second generation peptides modulating cellular adiponectin receptor responses. *Front Chem.* **2**, 93.

Otvos L. (2019). Potential adiponectin receptor response modifier therapeutics. *Front Endocrinol.* **10**, 539.

Pajvani UB, Du X, Combs TP, Berg AH, Rajala MW, Schulthess T, Engel J, Brownlee M, Scherer PE. (2003). Structure-function studies of the adipocyte-secreted hormone Acrp30/adiponectin. Implications for

- metabolic regulation and bioactivity. *J Biol Chem.* **278**, 9073-9085.
- Park T, Baek M, Lee H, Seok C. (2019). GalaxyTongDock: symmetric and asymmetric ab initio protein-protein docking web server with improved energy parameters. *J Comput Chem.* **40**, 2413-2417.
- Pischon T, Girman CJ, Hotamisligil GS, Rifai N, Hu FB, Rimm EB. (2004). Plasma adiponectin levels and risk of myocardial infarction in men. *JAMA.* **291**, 1730-1737.
- Price VH. (1999). Treatment of hair loss. *N Engl J Med.* **341**, 964-973.
- Shibata S, Tada Y, Asano Y, Hau CS, Kato T, Saeki H, Yamauchi T, Kubota N, Kadowaki T, Sato S. (2012). Adiponectin regulates cutaneous wound healing by promoting keratinocyte proliferation and migration via the erk signaling pathway. *J Immunol.* **189**, 3231-3241
- Sievers F, Wilm A, Dineen D, Gibson TJ, Karplus K, Li W, Lopez R, McWilliam H, Remmert M, Söding J, Thompson JD, Higgins DG. (2011). Fast, scalable generation of high-quality protein multiple sequence alignments using Clustal Omega. *Mol Syst Biol.* **7**, 539.
- Singh AK, Joharapurkar AA, Khan MP, Mishra JS, Singh N, Yadav M, Hossain Z, Khan K, Kumar S, Dhanesha NA, Mishra DP, Maurya R, Sharma S, Jain MR, Trivedi AK, Godbole MM, Gayen JR, Chattopadhyay N, Sanyal S. (2014). Orally active osteoanabolic agent GTDF binds to adiponectin receptors, with a preference for AdipoR1, induces adiponectin-

associated signaling, and improves metabolic health in a rodent model of diabetes. *Diabetes*. **63**, 3530-3544.

Straub LG, Scherer PE. (2019). Metabolic messengers: adiponectin. *Nat Metab*. **1**, 334-339.

Tanabe H, Fujii Y, Okada-Iwabu M, Iwabu M, Nakamura Y, Hosaka T, Motoyama K, Ikeda M, Wakiyama M, Terada T, Ohsawa N, Hato M, Ogasawara S, Hino T, Murata T, Iwata S, Hirata K, Kawano Y, Yamamoto M, Kimura-Someya T, Shirouzu M, Yamauchi T, Kadowaki T, Yokoyama S. (2015). Crystal structures of the human adiponectin receptors. *Nature*. **520**, 312-316.

Thi Mong Diep Nguyen. (2020). Adiponectin: Role in Physiology and Pathophysiology. *Int. J. Prev. Med*. **11**, 136.

Tomas E, Tsao TS, Saha AK, Murrey HE, Zhang CC, Itani SI, Lodish HF, Ruderman NB. (2002). Enhanced muscle fat oxidation and glucose transport by ACRP30 globular domain: acetyl-CoA carboxylase inhibition and AMP-activated protein kinase activation. *Proc Natl Acad Sci USA*. **99**, 16309-16313.

Tsao TS, Tomas E, Murrey HE, Hug C, Lee DH, Ruderman NB, Heuser JE, Lodish HF. (2003). Role of disulfide bonds in Acrp30/ adiponectin structure and signaling specificity. Different oligomers activate different signal transduction pathways. *J Biol Chem*. **278**, 50810-50817.

Vasiliauskaitė-Brooks I, Sounier R, Rochaix P, Bellot G, Fortier M, Hoh F, De Colibus L, Bechara C, Saied EM, Arenz C, Leyrat C, Cranier S. (2017). Structural insights into adiponectin receptors suggest ceramidase activity. *Nature*. **544**, 120-123.

Waki H, Yamauchi T, Kamon J, Ito Y, Uchida S, Kita S, Hara K, Hada Y, Vasseur F, Froguel P, Kimura S, Nagai R, Kadowaki T. (2003). Impaired multimerization of human adiponectin mutants associated with diabetes: Molecular structure and multimer formation of adiponectin. *J Biol Chem*. **278**, 40352-40363.

Wang Y, Lam KS, Yau MH, Xu A. (2008). Post-translational modifications of adiponectin: Mechanisms and functional implications. *Biochem J*. **409**, 623-633.

Wang SJ, Lu WY, Liu KY. (2017). Adiponectin receptor agonist AdipoRon suppresses adipogenesis in C3H10T1/2 cells through the adenosine monophosphate-activated protein kinase signaling pathway. *Mol Med Rep*. **16**, 7163-9.

Wong GW, Wang J, Hug C, Tsao TS, Lodish HF. (2004). A family of Acrp30/adiponectin structural and functional paralogs. *Proc Natl Acad Sci USA*. **101**, 10302-10307.

Won CH, Yoo HG, Park KY, Shin SH, Park WS, Park PJ, Chung JH, Kwon OS, Kim KH. (2012). Hair growth-promoting effects of adiponectin in

vitro. *J Invest Dermatol.* **132**, 2849-2851.

Wood AJJ, Rittmaster RS. (1994). Finasteride. *N Engl J Med.* **330**, 120–125.

Yamauchi T, Kamon J, Ito Y, Tsuchida A, Yokomizo T, Kita S, Sugiyama T, Miyagishi M, Hara K, Tsunoda M, Murakami K, Ohteki T, Uchida S, Takekawa S, Waki TH, Tsuno NH, Shibata Y, Terauchi Y, Froguel P, Tobe K, Koyasu S, Taira K, Kitamura T, Shimizu T, Nagai R, Kadowaki T. (2003). Cloning of adiponectin receptors that mediate antidiabetic metabolic effects. *Nature.* **423**, 762-769.

Yamauchi T, Nio Y, Maki T, Kobayashi M, Takazawa T, Iwabu M, Okada-Iwabu M, Kawamoto S, Kubota N, Kubota T, Ito Y, Kamon J, Tsuchida A, Kumagai K, Kozono H, Hada Y, Ogata H, Tokuyama K, Tsunoda M, Ide T, Murakami K, Awazawa M, Takamoto I, Froguel P, Hara K, Tobe K, Nagai R, Ueki K, Kadowaki T. (2007). Targeted disruption of AdipoR1 and AdipoR2 causes abrogation of adiponectin binding and metabolic actions. *Nat Med.* **13**, 332-339.

Yamauchi T, Iwabu M, Okada-Iwabu M, Kadowaki T. (2014). Adiponectin receptors: A review of their structure, function and how they work. *Best Pract Res Clin Endocrinol Metab.* **28**, 15-23

Chapter 2.

**Structural insights into functions and assembly of
mitochondrial creatine kinase heteromeric complex**

2.1. Introduction

2.1.1. Background of CKMT

The presence of tissue and compartment-specific isoenzymes of creatine kinase (CK) is an important characteristic of this well-known enzyme (Kuby et al, 1954) and is critical to its functions in cellular energy metabolism. Most vertebrate tissues express two mitochondrial creatine kinase isoenzymes, which is CKMT1 and CKMT2 (Schlegel et al, 1988). CKMT1 has been detected in most other tissues like brain, kidney and sperm, while CKMT2 is found in striated muscle (Schlegel et al, 1988; Wallimann et al, 1994). CKMT exists in the intermembrane space of mitochondria by forming an octamer, and plays a role in cellular energy homeostasis (Dzeja et al, 2003; Wallimann et al, 1992; Saks et al, 1996). Both isoenzymes contribute to the formation of a substantial intracellular pool of phosphocreatine, which acts as a temporal energy buffer and prevents a quick drop in global ATP concentrations. Additionally, creatine diffuses into the mitochondria and couples with ATP produced from oxidative phosphorylation and the adenine nucleotide translocator (ANT) via CKMT (**Figure 2.1**)

In previous studies, the X-ray crystal structure of CKMT was reported (Fritz-Wolf et al, 1996; Eder et al, 2000). In contrast to dimeric cytosolic CK, CKMT not only forms dimers, but also associates into octamers. The octameric species is the predominant oligomeric form *in vitro* as well as *in*

vivo. The highly ordered, large cuboidal octamer has overall dimensions of about $105 \times 105 \times 86 \text{ \AA}$ and displays 422 point group symmetry. It assembles from four elongated “banana-shaped” dimers that are arranged around its fourfold axis. Along this axis, a central channel of about 20 \AA diameter extends through the entire octamer. The N-terminus of all monomers protrude into this channel. The top and bottom faces that are perpendicular to the fourfold octamer axis each expose the C-terminus of four monomers (**Figure 2.2**).

As shown in Figure 2.2, CKMT forms an octamer by forming an interface between one dimer and neighboring dimers. Accordingly, the dimer-dimer interface is quite important for octamer stability, and there are regions involved in this dimer-dimer interface: N-terminus (involved in residue 6, 7 and 9) and a predominantly hydrophobic patch around tryptophan 264 (involved in 145-155) (**Figure 2.3**). Earlier studies had already shown a key role of N-terminal amino acids and Trp264 for octamer stability, using site directed mutagenesis (Gross et al, 1994; Kaldis et al, 1994; Khuchua et al, 1998). Therefore, based on previous studies, the basis of the dimer-dimer interface is a hydrophobic patch, which is strengthened by numerous polar interactions.

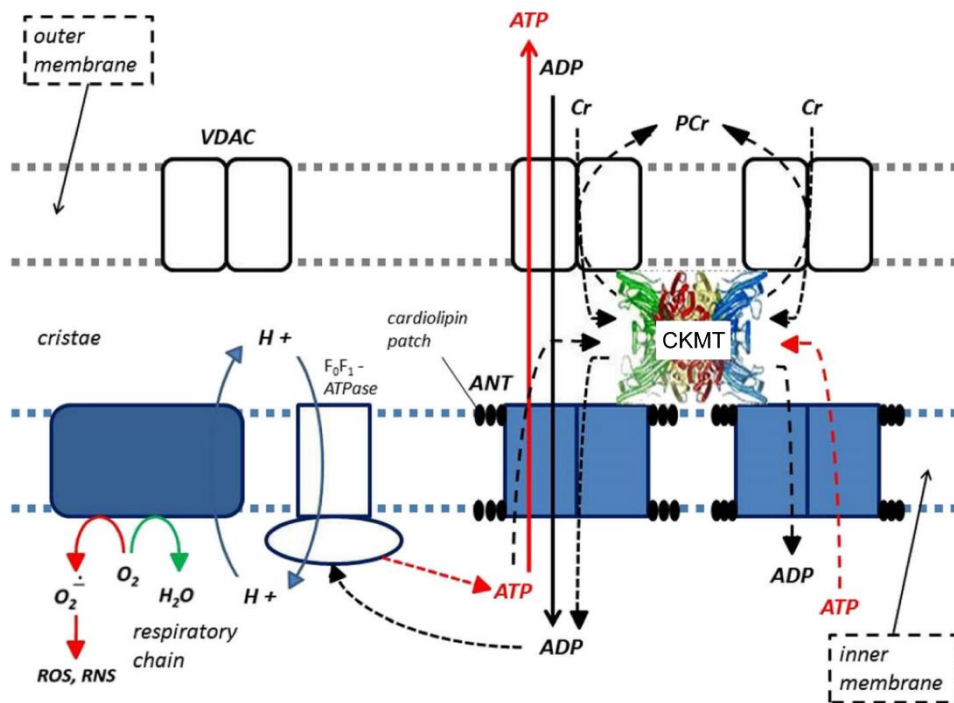


Figure 2.1 Role of CKMT in high energy metabolite transport and cellular respiration

VDAC = voltage-dependent anion channel; ROS = reactive oxygen species; RNS = reactive nitrogen species; ANT = adenine nucleotide translocator; ATP = adenine triphosphate; ADP = adenine diphosphate; Cr = creatine; and, PCr = phosphocreatine. This figure adapted from Kreider RB et al. 2017. International Society of Sports Nutrition position stand: safety and efficacy of creatine supplementation in exercise, sport, and medicine. *J Int Soc Sports Nutr.* **14**, 18

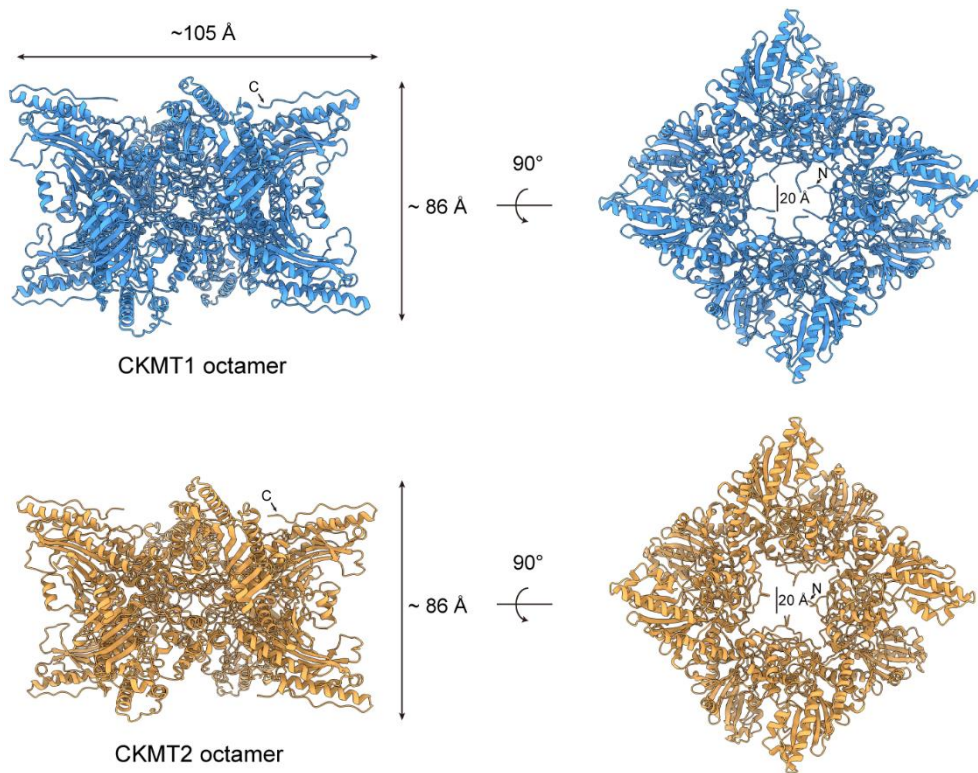


Figure 2.2 Molecular architecture of CKMT1 and CKMT2

The octameric structure of CKMT1 (1qk1, Eder et al, 2000) and CKMT2 (1crk, Fritz-Wolf et al, 1996). The side views (left) show a two-fold symmetry, and the top bottom views (right) reveal a 4-fold rotational symmetry of the dimers arranged around a 20 Å large central channel. The arrows indicate one of the eight N-terminus and one of the eight C-terminus.

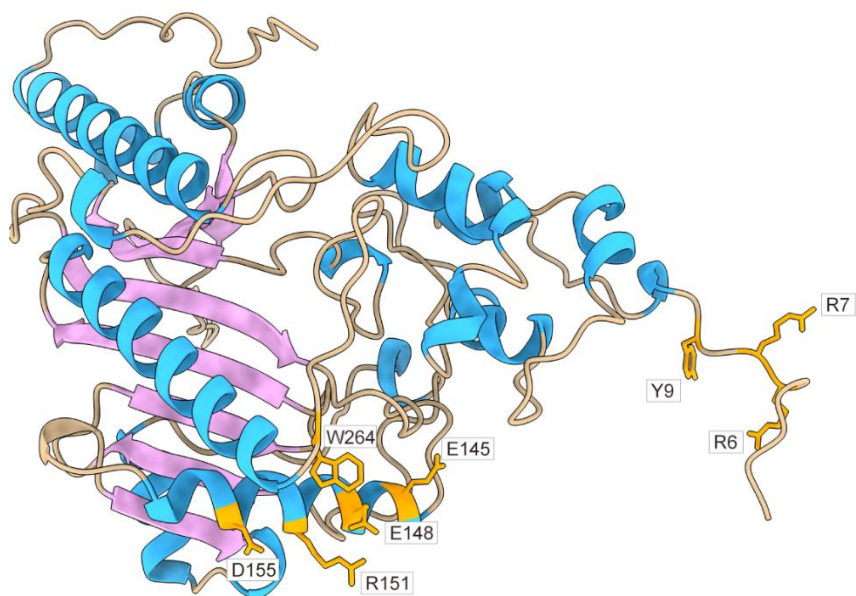


Figure 2.3 CKMT1 residues involved in octamer stability.

Cartoon diagram of a CKTM1 monomer colored according to secondary structure (α -helices in blue, β -sheets in pink) with side chains of key residues (orange) involved in dimer-dimer interaction.

2.1.2. Expression correlation of CKMT1 and CKMT2

For decades, many researchers have tried to describe the intracellular environment using genomic, transcriptomic, and proteomic techniques. Those techniques can identify components involved in biological processes to changing subcellular environment. Especially, proteomics is a powerful technique to understand many aspects of cellular network in specific cell, tissue, or organism (Cui et al, 2022). It offers supporting information to biological systems including cell signaling, metabolite pathway, protein expression and protein-protein interactions.

In contrast to DNA and RNA expression, protein-level correlation is related to protein interactions and functional similarity (Ryan et al, 2017). This observation is consistent with CCLE proteomic data analysis, which is positive expression correlations contribute to form protein complexes between similar mechanistic proteins (Nusinow et al, 2020). Therefore, we investigated the expression of CKMT1 and CKMT2 in CCLE proteomic data because CKMT1 and CKMT2 have similar functions. Interestingly, the Pearson correlation values of CKMT1 and CKMT2 were high, which means that CKMT1 and CKMT2 have an expression correlation (**Figure 2.4**). Based on these analyzes, we hypothesized that CKMT1 and CKMT2 would form a heteromeric complex.

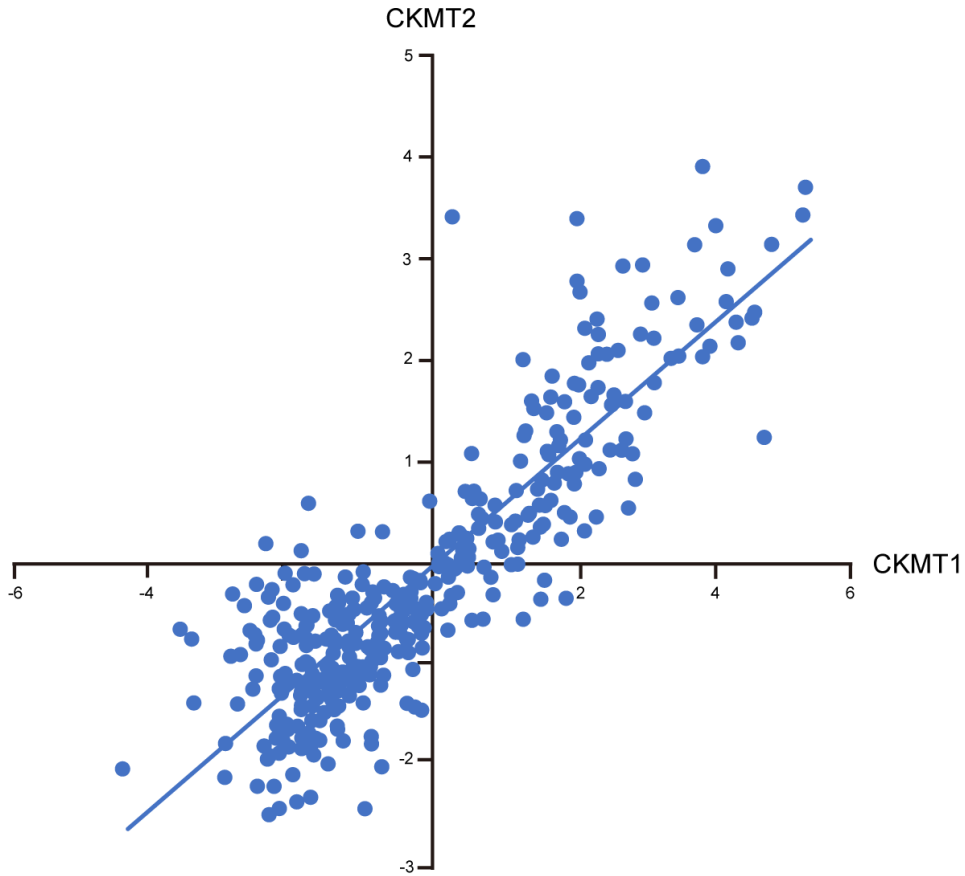


Figure2.4 [Ⓒ]Expression correlation of CKMT1 and CKMT2

Analysis of 369 cancer proteome data provided by Steven P. Gygi's group (Nusinow DP et al. 2022. Quantitative proteomics of the cancer cell line encyclopedia. *Cell*. 180, 387–402.). Blue dots represent different cancer cell lines.

[Ⓒ] Proteomic data analysis was performed by Jiwoong Kang in Seoul National University

2.1.3. Creatine-dependent thermogenesis

Creatine cycling has recently been revealed to contribute significantly to thermogenesis in beige adipocytes, one of the developing pathways implicated in thermogenesis (Kazak et al, 2015). Previously, researchers discovered an increase in mitochondrial-type creatine kinase in the BAT of cold-exposed rats. (Watanabe et al, 2008). Using proteomic analysis of mitochondria, Kazak et al. identified arginine–creatine metabolism as a specific signature of beige adipocytes in mice. Short-term cold exposure (6 h) dramatically increased gene expression and protein levels of creatine kinase CKMT1 and CKMT2 primarily in beige adipose tissue. Moreover, the addition of creatine to mitochondria from beige adipocytes stimulated respiration when levels of ADP were limiting respiration. This effect was not seen in mitochondria from muscle or brown adipocytes. In vivo inhibition of creatine transport reduced catecholamine-stimulated whole-body oxygen consumption by decreasing beige adipose tissue respiration (Kazak et al, 2015). Moreover, *Ckmt1* gene expression was upregulated in the beige adipose tissue of *Ucp1*-knockout mice, which indicates a compensatory role for creatine-cycling-mediated thermogenesis in the absence of UCP1. Blocking creatine transport in cultured human brown adipocytes nearly halved oxygen consumption, and small interfering RNA-mediated knockdown of CKMT1 also diminished respiration (Kazak et al, 2015). These findings are in line with studies in human beige adipose tissue samples, which indicated increased expression of the mitochondrial creatine kinase CKMT1

(Svensson et al, 2011), as well as with a more recent proteomic analysis of human brown/beige adipose tissue, which revealed an enrichment of the mitochondrial creatine kinases CKMT1A, CKMT1B and CKMT2 in parallel with UCP1 (Muller et al, 2016). More recently, it was demonstrated by patch clamp analysis of the internal mitochondrial membrane that UCP1-negative adipocytes within beige adipose tissue depots use creatine cycling as a thermogenic mechanism (Bertholet et al, 2017). Thus, beige adipocytes could contribute to non-shivering thermogenesis even in the absence of UCP1. **Figure 2.5** gives a conceptual overview of the proposed mechanisms of creatine cycling.

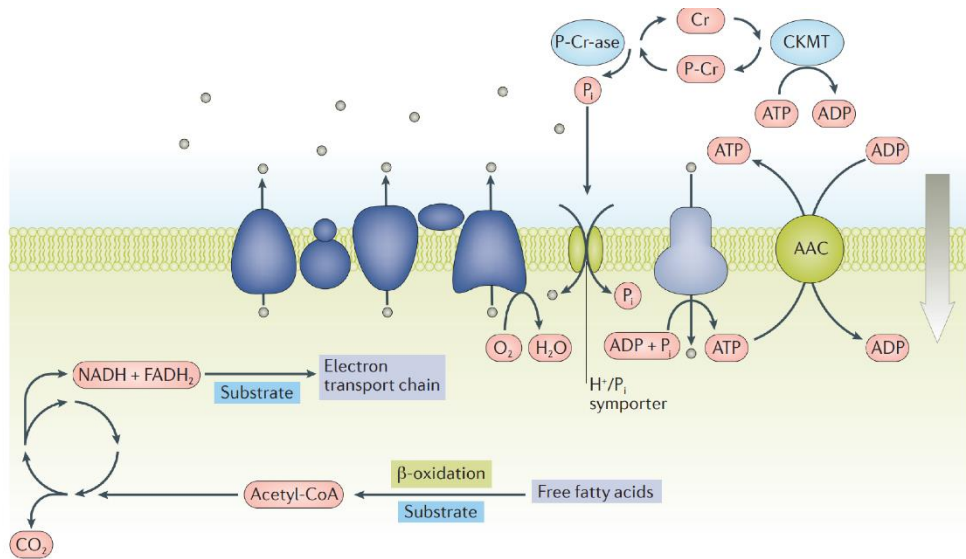


Figure 2.5 Creatine cycling model

CKMT transfers an activated phosphate from ATP to creatine (Cr), which forms phosphor-creatine (P-Cr). The resulting ADP is transferred into the mitochondrial matrix and drives oxidative phosphorylation. The P-Cr is hydrolysed by P-Cr-ase and is available for another futile cycle. This figure is adapted from Betz MJ & Enerback S. 2018. Targeting thermogenesis in brown fat and muscle to treat obesity and metabolic disease. *Nat. Rev. Endocrinol.* **14**, 77–87.

2.2. Materials and methods

2.2.1. Expression and purification of CKMT

The cDNAs encoding human WT CKMT1 (residues 39–412) and human WT CKMT2 (residues 40–413) were cloned into the pRSF duet vector, which introduced N-terminal 6xhis tag and strep tag, respectively. WT CKMTs were expressed in *E. coli* Rosetta2 (DE3) cells and induced with 0.5 mM isopropyl- β -D-1-thiogalactopyranoside (IPTG) at 25°C for 18 h, followed by growth to mid-log phase at 37°C. WT CKMT expressed-cell pellets were resuspended in lysis buffer (20 mM Tris-HCl pH 8.0, 500 mM NaCl, 5 mM 2-mercaptoethanol) containing 1 mM phenylmethylsulfonyl fluoride. Cells were lysed with a microfluidizer (Microfluidics, Westwood, MA, USA), and the lysed cells were centrifuged at 15000 x rpm for 30 min at 4°C. To purify WT CKMT heteromeric complex, we used Ni-sepharose resin (GE Healthcare) followed by strep-tactin sepharose resin (IBA Lifesciences) to remove homomeric complexes. The final eluate was purified by gel filtration on a Superpose 200 Increase 10/300 GL column (GE Healthcare) that had been pre-equilibrated with buffer containing 20 mM Tris-HCl pH 8.0, 200 mM NaCl and 5 mM 2-mercaptoethanol. We collected only the elution fractions corresponding to the homogenous octamer peak and proceeded with subsequent experiments. W213A CKMT construct was expressed and purified as described above.

2.2.2. In gel digestion and mass spectrometry analysis

SEC fractions of CKMT heteromeric complex were separated on 12% SDS–PAGE and stained with Coomassie blue. Protein gel slices were excised, washed with 1:1 acetonitrile:100 mM ammonium bicarbonate (v/v) for 30 min, dehydrated with 100% acetonitrile for 10 min, and dried in a speed-vac for 10 min without heat. Gel slices were reduced with 5 mM DTT for 30 min at 56 °C and then alkylated with 11 mM iodoacetamide for 30 min at room temperature in the dark. Gel slices were washed with 100 mM ammonium bicarbonate and 100% acetonitrile for 10 min each, and excess acetonitrile was removed by drying in a speed-vac for 10 min without heat. Gel slices were then rehydrated in a solution of 25 ng μl^{-1} trypsin in 50 mM ammonium bicarbonate for 30 min on ice, and trypsin digestions were performed overnight at 37°C. Digested peptides were collected and further extracted from gel slices in mass spectrometry (MS) extraction buffer (1:2 5% formic acid:acetonitrile (v/v)) with high-speed shaking. Supernatants were dried down in a speed-vac, and peptides were dissolved in a solution containing 0.1% formic acid. For MS analysis, one scan cycle is composed of a full-scan MS survey spectrum followed by CID and ETD. Full-scan MS spectra (400–2000, m/z) were acquired in the FT-Orbitrap at a resolution of 120 000, while CID-MS/MS spectra were recorded in IonTrap and ETD-MS/MS spectra were recorded in the FT-Orbitrap at a resolution of 30 000. Raw mass spectrometric data were processed and searched using the Sequest HT search engine within

the Proteome Discoverer 2.3 software (Thermo Scientific) with custom sequences.

2.2.3. Negative staining

WT CKMT and W213A CKMT samples were stained with uranyl acetate solution (~1% w/v) and examined by the FEI Tecnai 12 electron microscope with an accelerating voltage of 120 kV at appropriate magnification and defocus. The electron micrographs were recorded on Gatan US4000 4Kx4K CCD.

2.2.4. Western blot analysis

The obtained CKMT was then separated by 12% SDS-PAGE and transferred to a polyvinylidene fluoride membrane (Amersham). The protein transferred membranes were incubated overnight with the specific antibodies. The following antibodies were used: his (#MA5-15739, 1:5,000; Thermo Fisher), strep (#2-1509-001, 1:1,000; IBA lifesciences), Then, the membranes were washed and incubated with anti-mouse IgG HRP-linked antibody (#7076, 1:5,000; Cell Signaling) at 25°C for 1 h. Antibody-antigen complexes detected by enhanced chemiluminescent substrate (Thermo Fisher) were captured and quantified by Amersham imager 680 systems (GE Healthcare).

2.2.5. X-ray data collection and refinement

Crystals of W213A CKMT heteromeric complex were grown at 293 K using

the hanging drop method by mixing 1 μ l of a 5 mg/ml solution of MtCK protein in 20 mM Tris-HCl pH 8.0, 200 mM NaCl, and 5 mM 2-mercaptoethanol with 1 μ l of reservoir solution consisting of 100 mM MES (pH 5.5), 200 mM MgCl₂, and 8%(w/v) PEG4000. The crystals were cryoprotected with paratone-N prior to flash-freezing in a liquid nitrogen stream for data collection. Crystals of W213A CKMT heteromeric complex were diffracted to a resolution of 3.40 Å, and the diffraction data were processed and scaled using the XDS software package. The crystal belonged to the space group I422 with unit cell parameters of a=142.40 Å, b =142.40 Å, and c=215.56 Å. Model building was completed by iterative cycles of manual rebuilding using the COOT program (Emsley & Cowtan, 2004) and computational refinement by REFMAC (Murshudov et al, 2011) and PHENIX programs (Adams et al, 2002). The R_{work}/R_{free} values of the model were 20.91/26.79%. The final model of W213A showed that 90.28% of the residues were in the preferred region of the Ramachandran plot and an additional 7% were in the allowed region. PyMOL (PyMOL Molecular Graphics System, <http://www.pymol.org>) and UCSF chimera X (Goddard et al, 2018) were used to generate all the figures. Statistics for data collection and refinement are provided in **Table 2.1**.

Table 2.1 Statistics for data collection and refinement

Data set	CKMT1/CKMT2 W213A
A. Data collection	
X-ray source	PLS-5C
X-ray wavelength (Å)	0.9789
Space group	I422
Unit cell length (<i>a</i> , <i>b</i> , <i>c</i> , Å)	142.40, 142.40, 215.56
Unit cell angle (α , β , γ , °)	90.00, 90.00, 90.00
Resolution range (Å)	50 ~ 3.40
Total / unique reflections	77541/28581
Completeness (%)	98.1 (98.8) ^a
Average <i>I</i> / σ (<i>I</i>)	7.4 (1.4) ^a
<i>R</i> _{merge} ^b (%)	11.3 (81.3) ^a
B. Model refinement statistics	
Resolution range (Å)	50-3.40
<i>R</i> _{work} / <i>R</i> _{free} ^c (%)	21.04 / 26.54
Number / average <i>B</i> -factor (Å ²)	
Protein nonhydrogen atoms	5764/88
R.m.s. deviations from ideal geometry	
Bond lengths (Å)	0.011
Bond angles (°)	1.330
Protein-geometry analysis	
Ramachandran preferred (%)	90.1
Ramachandran allowed (%)	9.6
Ramachandran outliers (%)	0.3

Footnotes for Table 2.1

^aValues in parentheses refer to the highest resolution shell.

^b $R_{\text{merge}} = \frac{\sum_{hkl} \sum_i |I_i(hkl) - \langle I(hkl) \rangle|}{\sum_{hkl} \sum_i I_i(hkl)}$, where *I*(*hkl*) is the intensity of reflection *hkl*, \sum_{hkl} is the sum over all reflections, and \sum_i is the sum over *i* measurements of reflection *hkl*.

2.2.6. Dynamic light scattering

Thermostability of CKMT was determined using dynamic light scattering (DLS) using a DynaPro Nanostar (Wyatt technology). CKMT samples at ~ 2.0 mg/ml in 20 mM Tris/HCl pH 8.0, 200 mM NaCl, 5 mM 2-mercaptoethanol were analyzed at 37°C, 42°C or 48°C. During the incubation time from 20 to 30 mins, we observed changes in the hydrodynamic radius of CKMT at every minute.

2.2.7. Creatine kinase activity and co-operativity analysis

CKMT activity was measured using a creatine kinase activity assay kit (ab155091; Abcam, Cambridge, UK) according to the manufacturer's instructions with minor modification and read using a microplate reader Synergy™ H1 (BioTek). During the measurement of pH-dependent creatine kinase activity, we utilized a buffer A consisting of 20 mM Tris-HCl (pH 8.0, 7.0, and 6.0), 200 mM NaCl, and 0.1 mg/ml BSA instead of the kinase buffer provided in the creatine kinase activity kit. 10 µl CKMT (~2 mg/ml) proteins added to 40 µl buffer A and then it was mixed 1:1 with prepared kit-provided “Reaction Mix” in 96 well plate. The kinetic assay was conducted in the microplate reader Synergy™ H1 at 25°C in the dark. The absorbance of the reaction was read at 450 nm every 1 min for a total of 10 min. Creatine kinase activity was calculated by determining the NADH produced in the sample wells to a standard curve. Using this information, the creatine kinase activity

was represented in units of $\mu\text{mol}/\text{min}/\text{ml}$. We also conducted co-operativity measurements following the same procedure as described above, but the ATP (Sigma) and creatine (Sigma) used in the Reaction Mix were prepared as stocks to achieve the concentrations specified in the research paper.

2.3. Results

2.3.1. Purification and identification of WT CKMT and W213A CKMT heteromeric complex

I investigated whether wild type CKMT (WT CKMT) forms a heteromeric complex *in vitro*. A 6xhis tag was added to the C-terminus of CKMT1 and a strep tag was added to the C-terminus of CKMT2 to purify the CKMT heteromeric complex. Tandem affinity chromatography to remove homomeric complexes was then carried out, followed by size exclusion chromatography (SEC) (**Figure 2.6**). The CKMT heteromeric complex elutes from the column as a homogenous peak (**Figure 2.7A**). SDS-PAGE and western blot analysis revealed that CKMT1 and CKMT2 co-eluted in the same peak fraction. Using the peak fraction and SDS-PAGE gel from figure 2.7A, I performed the negative staining experiment and mass spectrometry analysis. As expected, the CKMT particles appear as an octamer with cube-like shapes, consistent with previous negatively stained electron micrographs (Furter et al, 1992) (**Figure 2.7B**). Additionally, peptides of CKMT1 and CKMT2 were detected in the mass spectrometry analysis (**Figure 2.8**). These results suggest that CKMT1 and CKMT2 reliably form a heteromeric complex *in vitro*.

To identify X-ray crystal structure of CKMT heteromeric complex, I attempted a crystallization experiment. Unfortunately, due to the high

sequence homology of CKMT1 and CKMT2 (**Figure 2.9**), there was a problem that the two proteins could not be distinguished without high resolution X-ray diffraction data (data not shown). Therefore, I introduced mutations to distinguish the two proteins. Among the five tryptophan residues in CKMT, tryptophan residue 213 was changed to alanine, which had no negative effects on the octamer formation or kinase activity (Gross et al, 1994) (**Figure 2.10**). The W213A CKMT heteromeric complex was purified in the same manner as the WT CKMT heteromeric complex purification method, and it was checked whether the introduced mutation had altered the octamer formation and kinase activity. As expected, W213A CKMT heteromeric complex could form an octamer and there was little difference in kinase activity changes by mutation compared to WT CKMT heteromeric complex (**Figure 2.11A and B**).

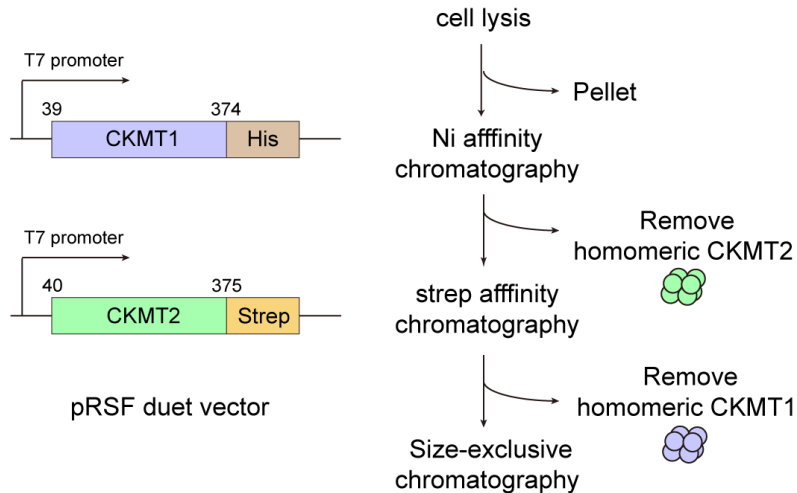


Figure 2.6 Schematic diagram for expression and purification of CKMT heteromeric complex

The cDNAs encoding human CKMT1 (residues 39–412) and human CKMT2 (residues 40–413) were cloned into the pRSF duet vector. To highly purify CKMT heteromeric complex, we used tandem affinity chromatography method. After cell lysis, Ni affinity chromatography and strep affinity chromatography were sequentially performed to remove the homomeric complex, and then the CKMT heteromeric complex was finally obtained through size-exclusion chromatography.

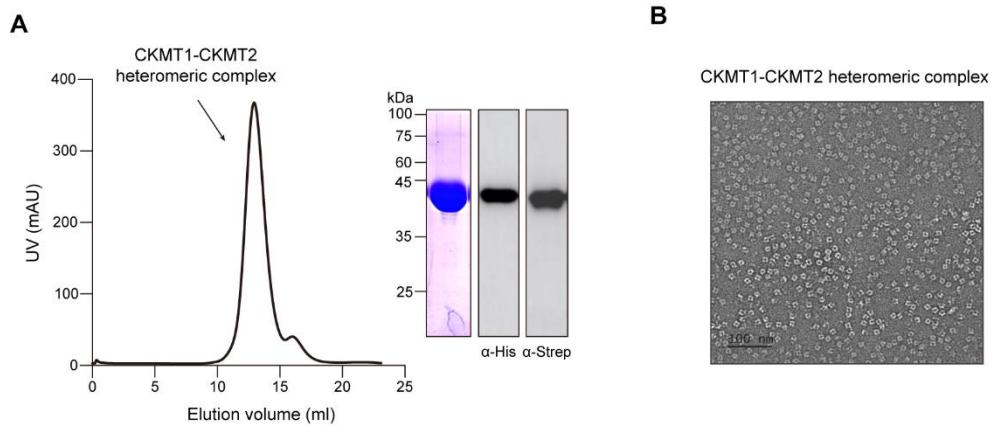


Figure 2.7 Purification of CKMT heteromeric complex and negative staining experiment

(A) Size-exclusion chromatography of WT CKMT heteromeric complex using Superpose 200 Increase 10/300 GL column, and purified heteromeric complex was shown on SDS-PAGE and western blot. (B) Negative stain electron microscopy image of WT CKMT1/2 heteromeric complex

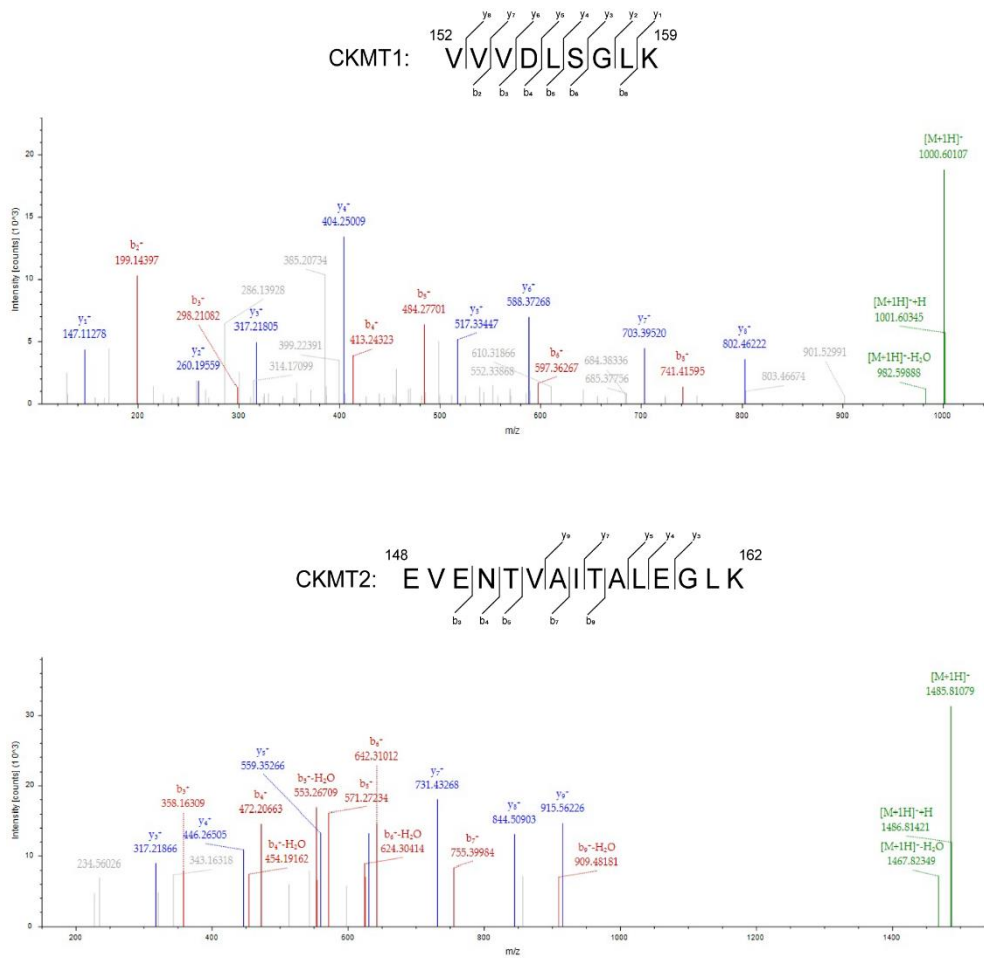


Figure 2.8 Representative LC-MS/MS spectrum of CKMT heteromeric complex

A piece of gel was cut from the SDS-PAGE in Figure 2.7 and analyzed by mass spectrometry.

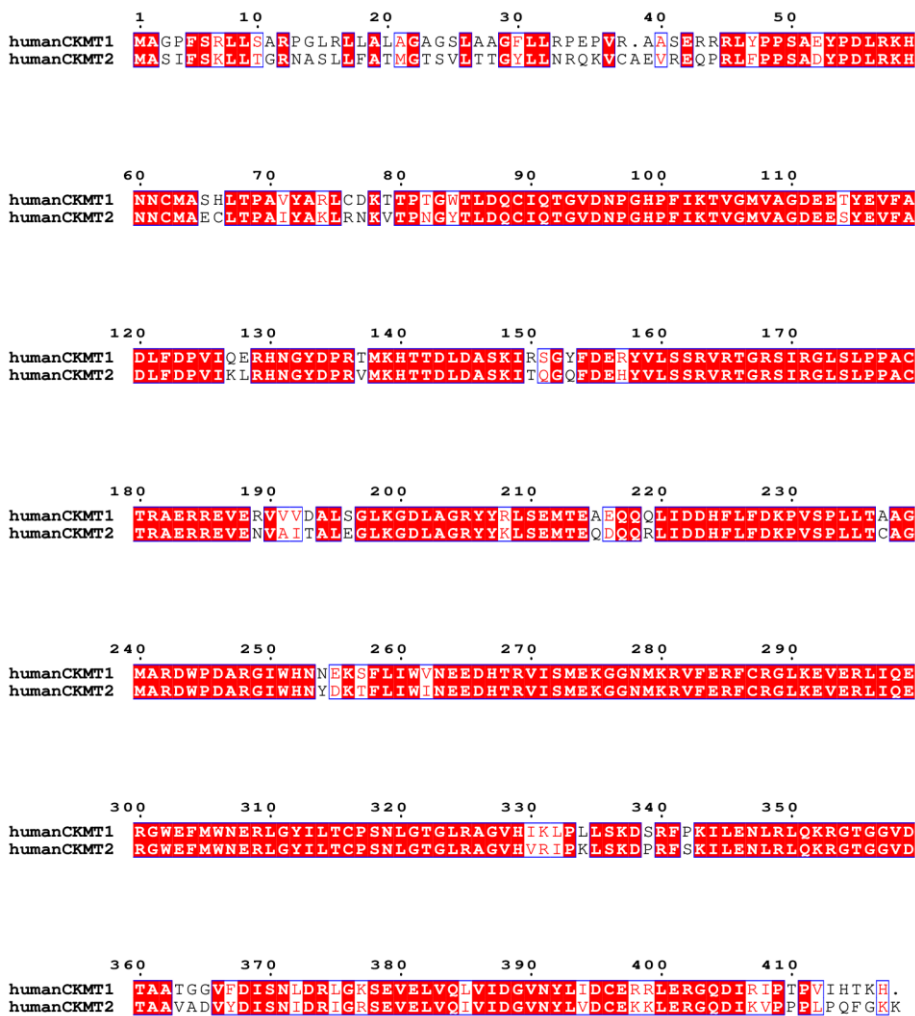


Figure 2.9 Sequence alignment of human CKMT1 (UniProtKB/Swiss-Prot accession number P12532) and human CKMT2 (UniProtKB/Swiss-Prot accession number P17540)

The alignment was performed using Clustal W (Larkin et al., 2007) and drawn with ESPrnt 3.0 (Robert and Gouet, 2014). Highly (100%) conserved residues are highlighted in red with white letters, and semi-conserved residues (80%) are highlighted in white with red letters.

```

      207                               219
      * * * * * * * * * * * * * * * * * *
CKMT1 :PDARGIWHNNNEKS
CKMT2 :PDARGIWHNYDKT
      ↓
      207                               219
      * * * * * * * * * * * * * * * * * *
CKMT1 :PDARGIWHNNNEKS
CKMT2 :PDARGIAHNYDKT

```

Figure 2.10 Sequence alignment of residues 207 to 219 of CKMT1 and CKMT2

The red box indicates the position of residue 213, and the residue where the mutation was introduced is indicated in bold.

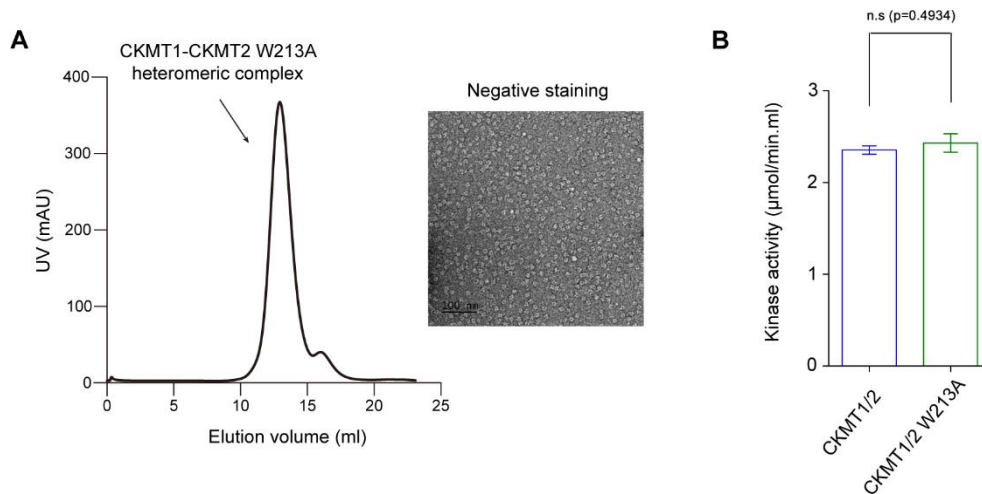


Figure 2.11 Purification of W213A CKMT heteromeric complex, negative staining experiment and creatine kinase activity test

(A) Size-exclusion chromatography of CKMT1/2 W213A heteromeric complex using Superpose 200 Increase 10/300 GL column and negative stain electron microscopy image of W213A CKMT heteromeric complex. (B) Creatine kinase activity of WT CKMT and W213A CKMT heteromeric complex

2.3.2. Overall structure of the CKMT heteromeric complex

I next determined the 3.4 Å X-ray crystal structure of W213A CKMT heteromeric complex containing the heteromeric dimer in asymmetry unit. First, I checked the electron density map of residue 213 to define CKMT1 and CKMT2 in the heteromeric dimer. Indeed, a clear difference was observed between the electron density map of tryptophan at position 213 of CKMT1 and the electron density map of alanine at position 213 of CKMT2 (**Figure 2.12A**). Therefore, I was able to define one of the heteromeric dimers as CKMT1 and the other as CKMT2. Furthermore, using the symmetry operation method, it was confirmed that CKMT1 and CKMT2 form a 4:4 stoichiometry in the heteromeric complex (**Figure 2.12B**).

Each monomer consists of a small N-terminus domain (domain I, residues 1-100) and a larger C-terminus domain (domain II, residues 113-end) connected by a long linker region without secondary structure (residues 101-112) (**Figure 2.13**). N-terminus region and flexible loop in residues 1-7 and 317-325 are disordered in both monomers. Weak density map was also found for the C-terminus (residues 362-374) and for some side chain of a flexible loop (residues 61-65). The small N-terminal domain is exclusively α -helical. It contains 6 conserved α -helices, and the core of the C-terminal large domain is formed by an eight-stranded antiparallel β -sheet, which is flanked by seven α -helices. The β -sheet has a saddle-like shape and is bended to about 120° (**Figure 2.14**).

When structural alignment was performed with the previously reported

homomeric complex structure, it was generally similar, but the domains of the heteromeric complex showed a slight inward bending (**Figure 2.15**). Not only this, when comparing the heteromeric octamer with the CKMT1 octamer and the CKMT2 octamer, due to the characteristics shown in the dimer, the vertical width of heteromeric octamer structure is wider than the CKMT1 octamer structure and less wide than the CKMT2 octamer structure (**Figure 2.16**). As Taken together, the overall structure of the heteromeric complex is similar to the CKMT2 structure, with CKMT1 and CKMT2 forming a 4:4 stoichiometry.

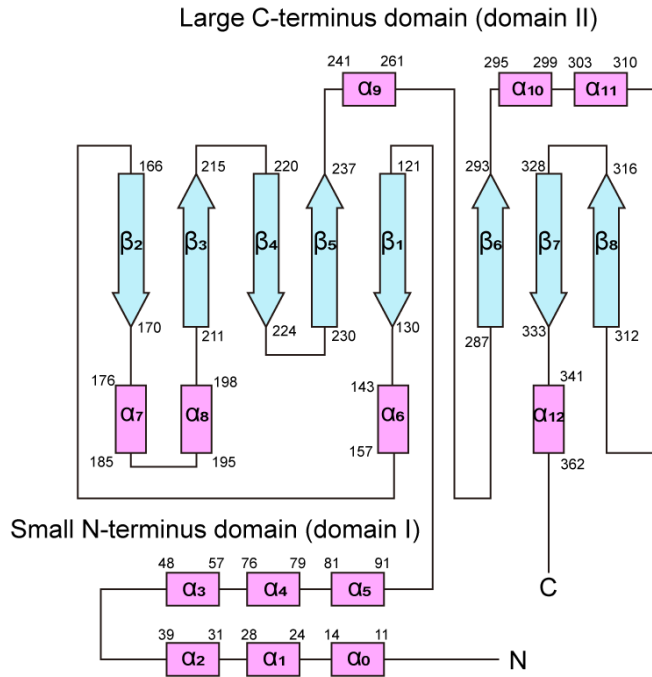


Figure 2.13 Schematic representation of the secondary structure of CKMT1

Domain architecture of CKMT1 monomer. The monomer of CKMT1 consist of small N-terminus domain (domain I) and large C-terminus domain (domain II). Alpha helices and beta sheet were indicated pink and cyan, respectively.

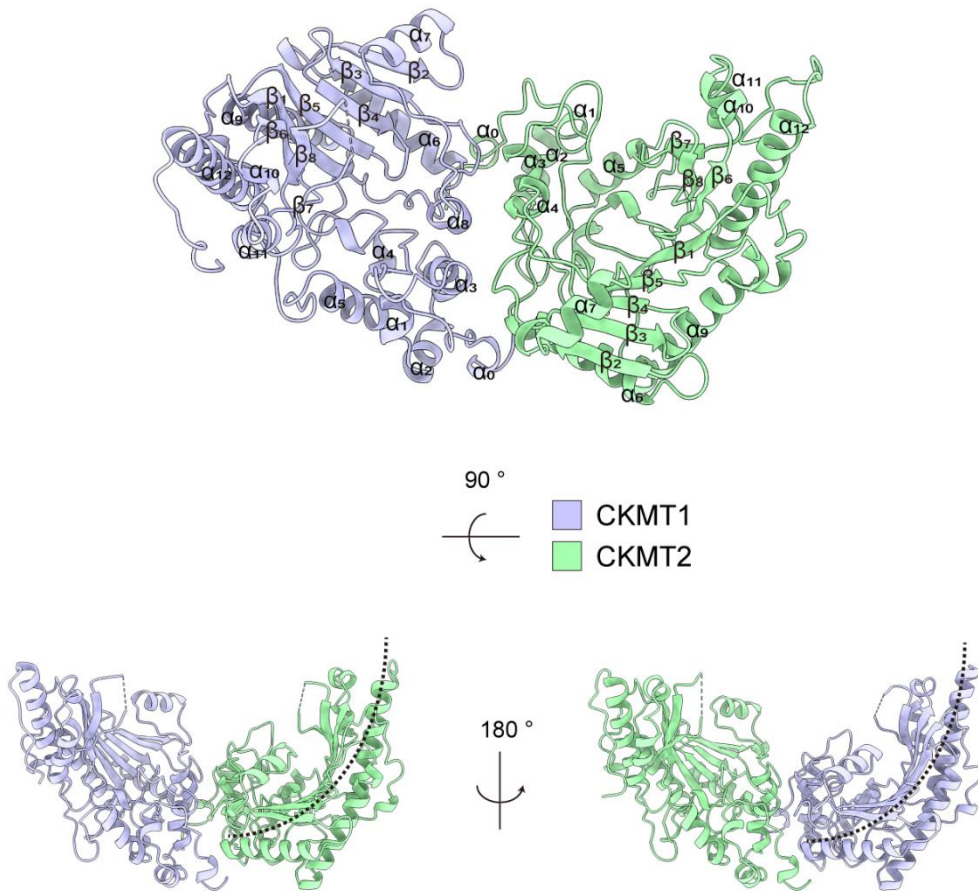


Figure 2.14 X-ray crystal structure of W213A CKMT heteromeric dimer
 Chain fold of CKMT heteromeric dimer. Schematic backbone representation of a CKMT heteromeric dimer showing the general chain fold with all secondary structure elements. The dashed line indicates that the β -sheet is bent.

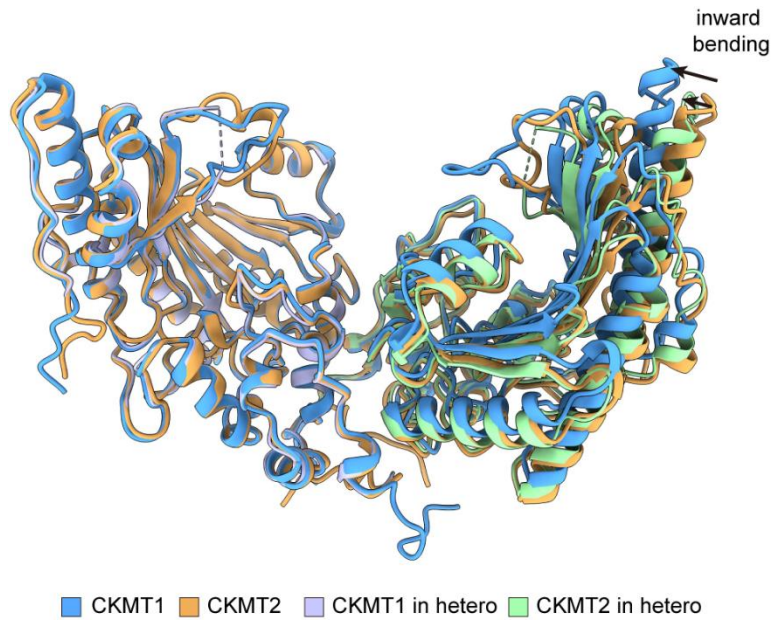


Figure 2.15 Superimposed structures of heteromeric dimer and homomeric dimer

Structure overlap based on one monomer, exhibiting an inward bending of the overall structure.

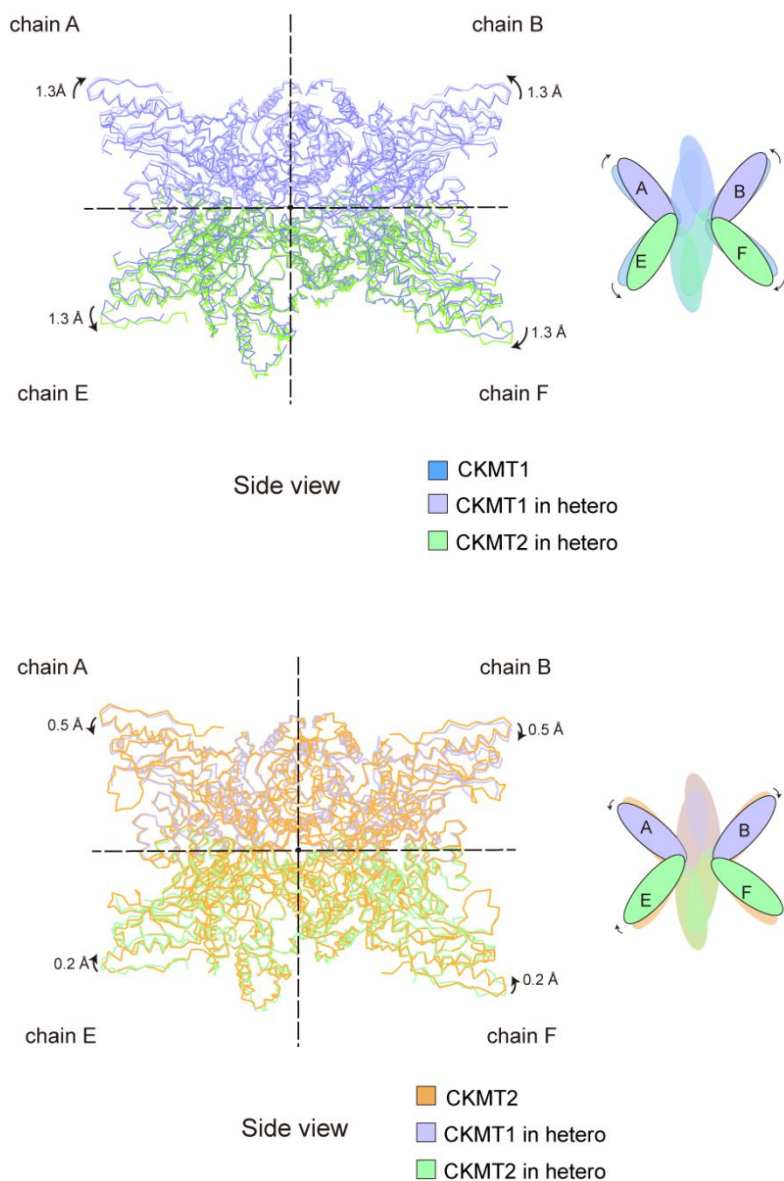


Figure 2.16 Comparison of octamer structures of CKMT

Superimposed structures of heteromeric octamer and homomeric octamer. After overlapping the structures, the structures observed from the side view were shown as a ribbon diagram.

2.3.3. Characterization of the CKMT heteromeric complex

Next, I attempted various experiments to identify functional differences in the heteromeric complex. According to previous studies, the specific creatine kinase activity of CKMT homomeric complexes varied depending on pH and cytosolic creatine kinase has co-operativity between different active sites in reverse reaction (Kaldis et al, 1995; Hornemann et al, 2000). Therefore, I investigated kinase activity of the heteromeric complex depending on pH and co-operativity. As shown in **figure 2.17A**, the kinase activity of the heteromeric complex was shown to increase as pH increased, similar to that of the homomeric complex. However, it was not possible to find a pH range in which the activity was better or worse than that of the homomeric complex. Additionally, there was no difference between the heteromeric complex and the homomeric complex in the co-operativity experiment with ATP (**Figure 2.17B**).

Biophysical analysis revealed that octamer dissociation can be triggered by changes in temperature (Gross et al, 1995). To further understand thermal stability of CKMTs, I investigated the thermal stability of the heteromeric complex and the homomeric complex using dynamic light scattering (DLS) analysis. As shown in **figure 2.18A**, dramatic aggregation of the heteromeric complex and homomeric complex was observed after 40°C, but the kinase activity stabilized until 50 °C and significantly decreased thereafter (**Figure 2.18B**). Furthermore, I measured thermal stability of CKMTs at 42 and 48°C, referring to a paper that suggest that temperature of intracellular active

mitochondria rises between 42 and 48°C (Okabe et al, 2012; Ruan et al, 2021). In an experiment measured at 48°C, aggregation of both the heteromeric complex and homomeric complex was seen to begin after 2 min. However, interestingly, in an experiment measured at 42 °C, the heteromeric complex was stable even after 20 min, whereas the homomeric complex began aggregation after 10 min (**Figure 2.19A and B**). Additionally, as a result of measuring the time-dependent kinase activity of the heteromeric complex at 42°C, the activity of heteromeric complex was maintained for up to 120 minutes while the homomeric complex showed a tendency for activity to decrease after 60 minutes (**Figure 2.19C**). These findings suggest that the heteromeric complex has better thermal stability than the homomeric complex.

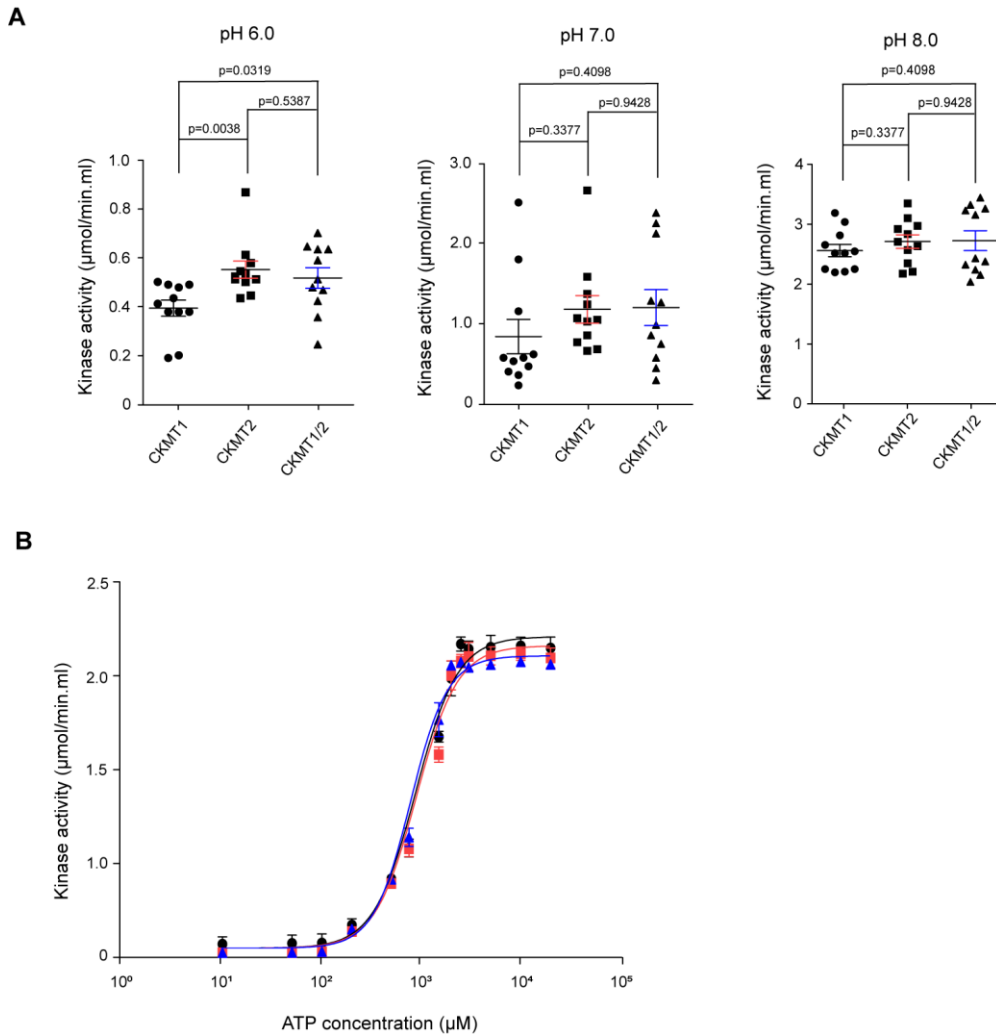


Figure 2.17 Functional characterization of CKMT *in vitro*

(A) pH-dependent kinase activity of CKMT, as indicated (n = 11 technical replicates/group). (B) Co-operativity test of CKMT on ATP, as indicated (n = 3 technical replicates/group).

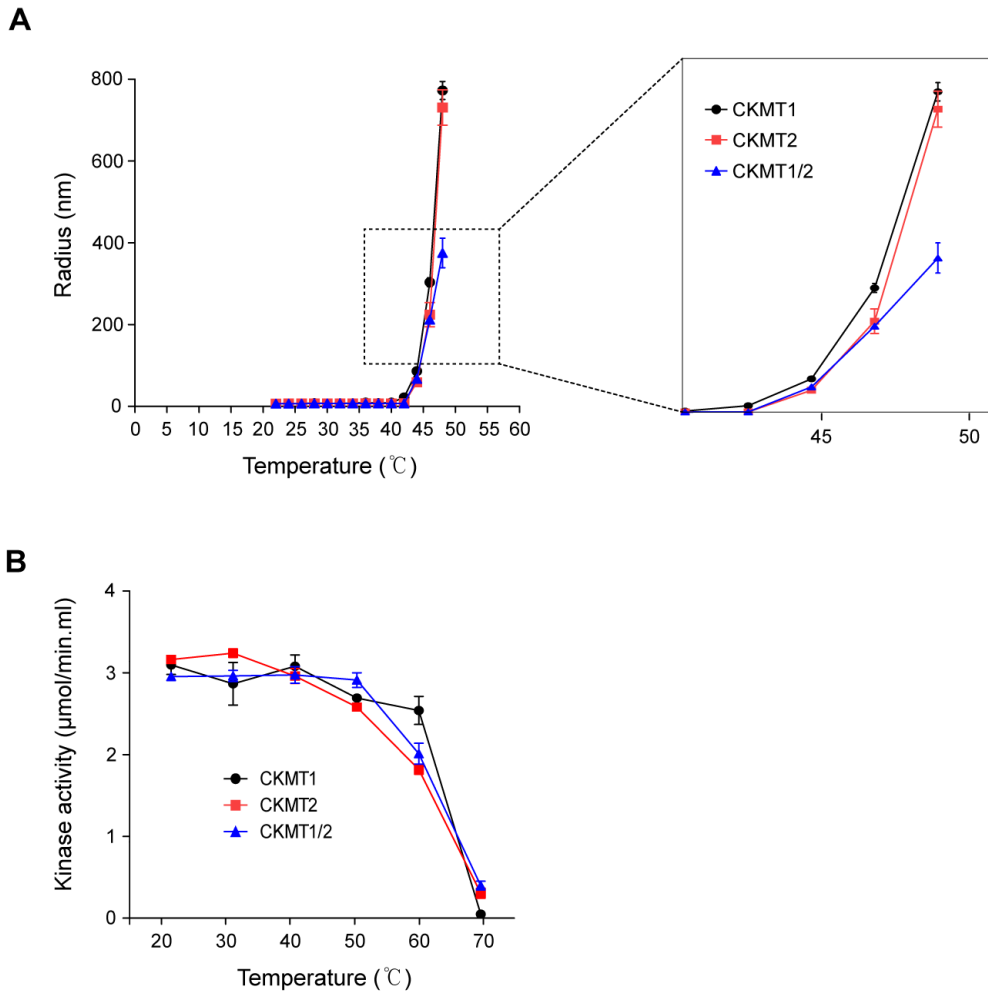


Figure 2.18 Thermal stability of CKMT complexes

(A) Thermal stability evaluation of CKMT complexes in temperature-dependent manner, as indicated (n=3 technical replicates/group). (B) Optimal temperature of CKMT complexes was determined by measuring the activities after incubating samples at 20-60°C for 10 min, as indicated (n=3 technical replicates/group).

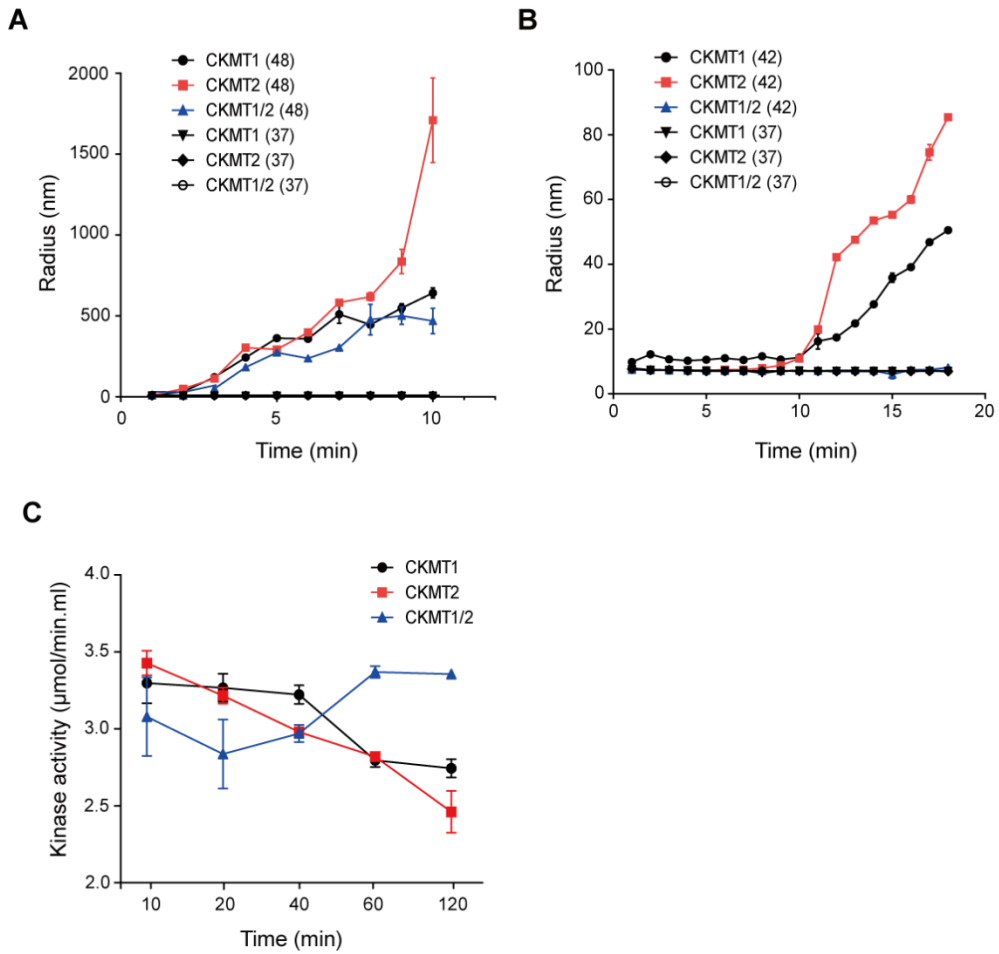


Figure 2.19 Thermal stability of CKMT complexes at 42 and 48°C, and a change in the kinase activity depending on time.

(A)-(B) Thermal stability of CKMT heteromeric complex in time-dependent manner, (n=3 technical replicates/group). (C) Change of kinase activity for CKMT complexes during 10-120 min at 42°C, as indicated (n=3 technical replicates/group).

2.3.4. Structural perspective on the reason for the high thermal stability of CKMT heteromeric complex

I tried to understand why heteromeric complexes had better thermal stability than homomeric complexes from a structural viewpoint. I thought that the high thermal stability of the heteromeric complex would mean that the octamer was stably formed. According to previous studies, two structural parts involved in octamer stability. The first part is the N-terminus contact region, and the second part is the hydrophobic patch and polar interaction around Trp264 (Gross et al, 1994; Kaldis et al, 1994; Khuchua et al, 1998). Two parts belong to the dimer-dimer interface.

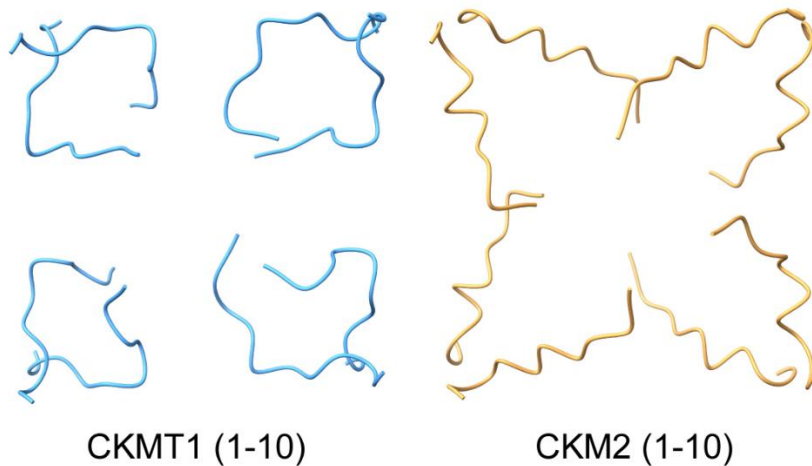
The N-terminus region is less conserved among CKMTs with quite high sequence homology (**Figure 2.20A**) and is where clear structural differences between CKMT1 and CKMT2 are observed (**Figure 2.20B**). The two N-terminus of an CKMT dimer extend from the monomer core, intertwine with the N-termini of the two neighboring dimers, and form extensive clamp-like contacts (Fritz-Wolf et al, 1996; Eder et al, 2000). Therefore, I made a chimera construct (**Figure 2.21A**) and checked whether there was an N-terminus effect on thermal stability. As shown in **figure 2.21B**, a chimera heteromeric complex, which the 8 N-terminus of the heteromeric complex were CKMT1, had the almost same thermal stability as the WT CKMT heteromeric complex. This suggests that N-terminus region in dimer-dimer interface does not significantly involve in thermal stability.

The dimer-dimer interface around Trp264 is greatly involved in octamer

stability. Hydrophobic patch around Trp264 is known to be a very important region in octamer formation, and when Trp264 was mutated, it was unable to form an octamer (Gross et al, 1994; Hoffman et al, 2006). However, when I analyze structural superimposition of CKMT complexes around Trp264, there were no change in the residue interactions and hydrophobicity (**Figure 2.22**). Nevertheless, Arg151 interact with Glu148 because $\alpha 6$ helix directly contact between neighboring dimer (**Figure 2.23A**). Therefore, I mutated arginine residue 151 to alanine and evaluated its thermal stability. I observed faster aggregation for the R151A heterocomplex than for the WT heterocomplex (**Figure 2.23B**). Consequently, Arg151 is very important residue for the thermal stability of heteromeric complex by forming stable octamer. However, this polar interaction in the heteromeric complex is not present in CKMT2 but is present in CKMT1. Unfortunately, although results of figure 2.23 could explain that the heteromeric complex has better thermal stability than CKMT2, it could not explain for CKMT1. In CKMT2, the arginine residues do not form any contacts with neighboring dimers. In CKMT1, Arg151 participates in two salt bridges with Glu148 and Asp155 located in the center of the dimer-dimer interface (**Figure 2.24**). So, further experiments are needed to investigate the interaction strength of the dimer-dimer interface.

A

human CKMT1	A	A	S	E	R	R	R	L	Y	P	P	S	A	E	Y	P	D	L	R	K	H	N	N	C	M	A	S
chicken CKMT1	A	G	E	R	Q	R	R	R	Y	P	P	S	A	E	Y	P	D	L	R	K	H	N	N	C	M	A	S
bovine CKMT1	A	A	S	E	R	R	R	L	Y	P	P	S	A	E	Y	P	D	L	R	K	H	N	N	C	M	A	S
mouse CKMT1	A	A	A	A	E	R	R	R	L	Y	P	P	S	A	E	Y	P	D	L	R	K	H	N	N	C	M	A
rat CKMT1	A	A	T	G	E	R	R	R	L	Y	P	P	S	A	E	Y	P	D	L	R	K	H	N	N	C	M	A
human CKMT2	A	E	V	R	E	Q	P	R	L	F	P	P	S	A	D	Y	P	D	L	R	K	H	N	N	C	M	A
chicken CKMT2	A	T	V	H	E	K	R	K	L	F	P	P	S	A	D	Y	P	D	L	R	K	H	N	N	C	M	A
bovine CKMT2	A	A	A	R	E	Q	H	K	L	F	P	P	S	A	D	Y	P	D	L	R	K	H	N	N	C	M	A
mouse CKMT2	A	D	A	R	E	Q	H	K	L	F	P	P	S	A	D	Y	P	D	L	R	K	H	N	N	C	M	A
rat CKMT2	A	D	A	R	E	Q	H	K	L	F	P	P	S	A	D	Y	P	D	L	R	K	H	N	N	C	M	A

B**Figure 2.20 Sequence alignment and structure comparison of N-terminus**

(A) Multi-alignment of the CKMTs from *Homo sapiens* (UniProtKB/Swiss-Prot accession number P12532 and P17540), *Gallus gallus* (UniProtKB/Swiss-Prot accession number P70079 and P11009), *Bos taurus* (UniProtKB/ Swiss-Prot accession number Q9TTK8 and Q3ZBP1), *Mus musculus* (UniProtKB/Swiss-Prot accession number P30275 and Q6P8J7), and *Rattus norvegicus* (UniProtKB/Swiss-Prot accession number P25809 and P09605). The alignment was performed using Clustal W (Larkin et al., 2007)

and drawn with ESPript (Robert and Gouet, 2014). Highly (100%) conserved residues are highlighted in red with white letters, and semi-conserved residues (80%) are highlighted in white with red letters. (B) N-terminus structure of CKMT1 and CKMT2 homomeric complex. The N-terminus structure of CKMT has a sickle-like shape, and the N-terminus structure of CKMT2 has a V-like shape.

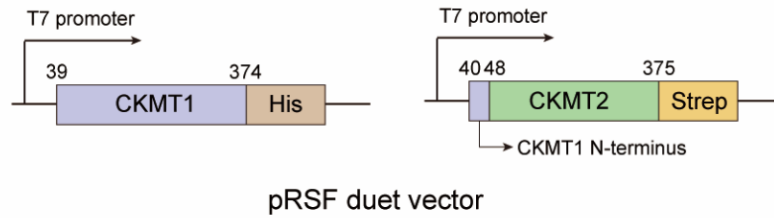
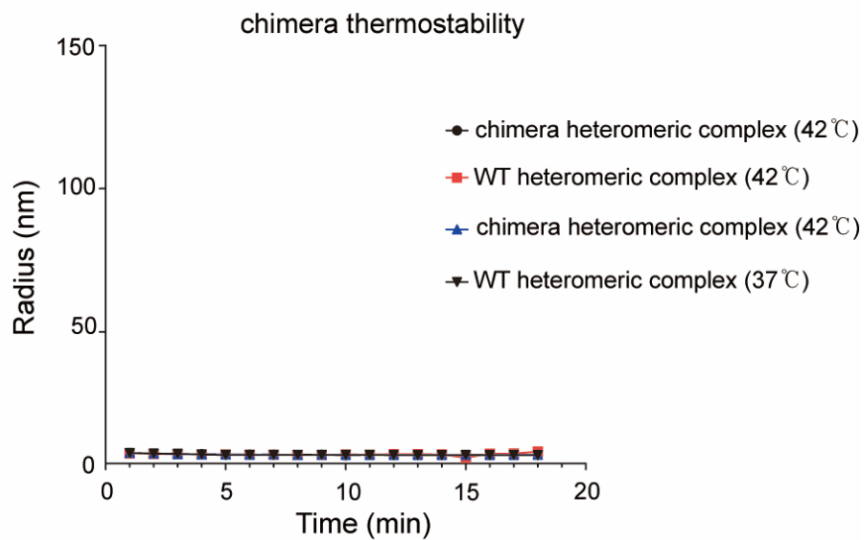
A**B**

Figure 2.21 Chimera construct design and thermal stability of chimera heteromeric complex

(A) The N-terminus region (VREQPRLF) of CKMT2 was replaced with the N-terminus region (ASERRRLY) of CKMT1. (B) Thermal stability of chimera heteromeric complex in time-dependent manner, (n=3 technical replicates/group).

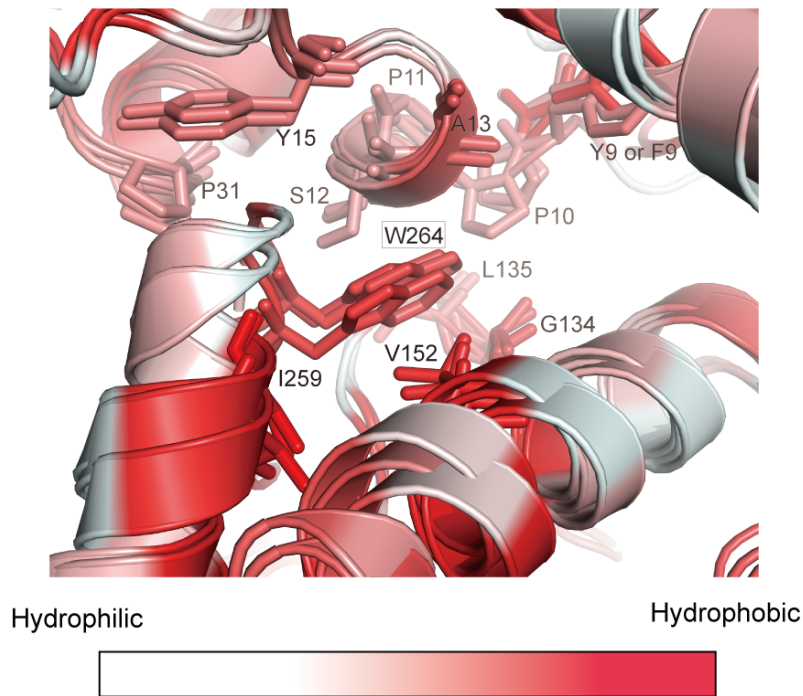
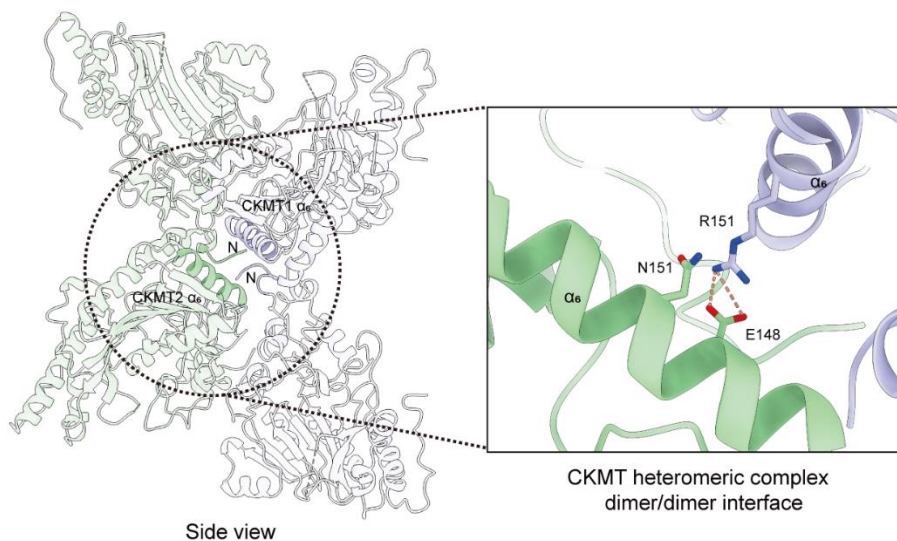


Figure 2.22 Interactions and hydrophobicity of residues around W264 -
 Structural overlap around W264 of CKMT1 (PDB ID: 1qk1), CKMT2 (PDB ID: 1crk), and heteromeric complex. The color of each residue is determined by the degree of hydrophobicity (white to red).

A



B

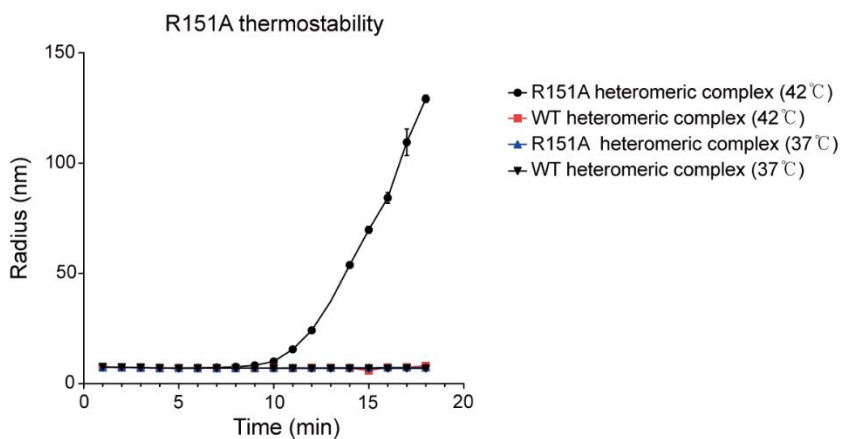
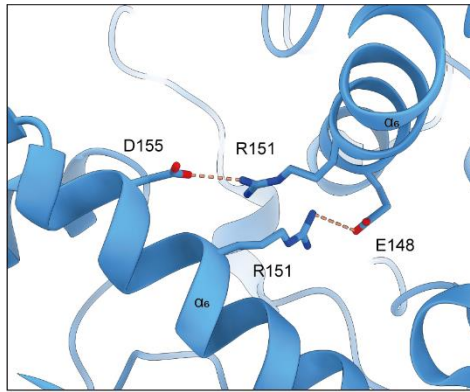
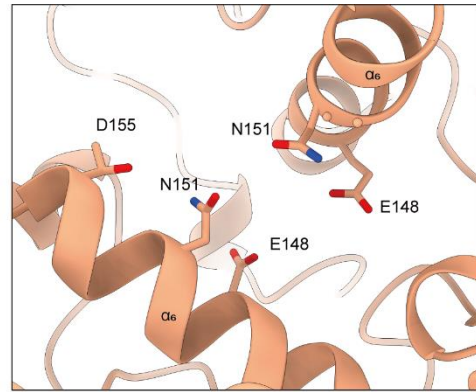


Figure 2.23 Dimer-dimer interface of heteromeric complex and thermal stability for R151A heteromeric complex

(A) The polar interaction at the dimer-dimer interface of heteromeric complex is shown as a cartoon diagram. (B) Thermal stability of R151A heteromeric complex in time-dependent manner, (n=3 technical replicates/group).



CKMT1 homomeric complex (1qk1)
dimer/dimer interaction



CKMT2 homomeric complex (1crk)
dimer/dimer interface

Figure 2.24 Dimer-dimer interface of CKMT1 and CKMT2 homomeric complex

The polar interaction at the dimer-dimer interface is shown as a cartoon diagram. Two polar interactions exist in CKMT1 (PDB ID: 1qk1) and do not exist in CKMT2 (PDB ID: 1crk).

2.4. Discussion

In this study, I determined the CKMT heteromeric structure that CKMT1 and CKMT2 form an octamer with 4:4 stoichiometry. When compared to the structures of previously reported homomeric complexes, the heteromeric complex was similar to the CKMT2 homomeric complex but had much better thermal stability. Although the structural interpretation of why the temperature stability is higher requires further analysis, the thermal stability of the heteromeric complex may have sufficient biological significance in cell or tissues, such as adipocyte.

Most recently, independent findings have suggested an entirely novel mechanism linking CKMT activity to thermogenesis. Adipocytes have been known to contain few if any CKMT1 (Streijger et al. 2009). However, more quantitative proteomics identified a strong upregulation of CKMT proteins in thermogenic adipocytes: human BAT as compared to white adipocytes (Svensson et al. 2011; Muller et al. 2016), and mouse beige adipocytes induced by cold exposure (Kazak et al. 2015). Most importantly, the latter study further provided evidence for a CKMT-driven thermogenic futile cycle. In this model, PCr generated by CKMT is not used for cellular work in the cytosol, but instead immediately hydrolyzed, thus increasing energy expenditure, and releasing heat energy. Released Cr is then rapidly rephosphorylated by CKMT with mitochondrial ATP, and the generated ADP

channeled into the matrix to stimulate respiration, a pathway corresponding to the classical CKMT bioenergetic function. Such creatine-driven cycling seems to be present at least in UCP1-positive and -negative beige adipocytes, but not in white adipocytes (Bertholet et al. 2017). Given these contents, I can hypothesize that heteromeric complex structure may require to maintain thermal stability within mitochondria, where the temperature rises owing to heat generation. To verify the hypothesis, it would be possible to conduct experiments to observe changes in cell viability or changes in mitochondrial activity by subjecting cells knocking down CKMT1 or CKMT2 to heat shock.

In summary, I successfully purified the CKMT heteromeric complex and solved its X-ray crystal structure. Based on the structural analysis and functional experiment evidence, I showed that the stoichiometry of CKMT1 and CKMT2 and heteromeric complex has significant thermal stability. Moreover, my findings may suggest the possibility of the existence of a previously unreported heteromeric complex that ensures stability against heat generation occurring in adipocytes.

2.5. References

- Adams PD, Grosse-Kunstleve RW, Hung LW, Ioerger TR, McCoy AJ, Moriarty NW, Read RJ, Sacchettini JC, Sauter NK, Terwilliger TC. (2002). PHENIX: building new software for automated crystallographic structure determination. *Acta Cryst. D.* **58**, 1948-1954.
- Bertholet AM, Kazak L, Chouchani ET, Bogaczynska MG, Paranjpe I, Wainwright GL, Bétourné A, Kajimura S, Spiegelman BM, Kirichok Y. (2017). Mitochondrial patch clamp of beige adipocytes reveals UCP1-positive and UCP1-negative cells both exhibiting futile creatine cycling. *Cell Metab.* **25**, 811-822.
- Betz MJ, Enerback S. (2018). Targeting thermogenesis in brown fat and muscle to treat obesity and metabolic disease. *Nat. Rev. Endocrinol.* **14**, 77-87.
- Cui M, Cheng C, Zhang L. (2022) High-throughput proteomics: a methodological mini-review. *Lab. Invest.* **102**, 1170-1181.
- Dzeja PP, Terzic A. (2003). Phosphotransfer networks and cellular energetics. *J. Exp. Biol.* **206**, 2039-2047.
- Eder M, Fritz-Wolf K, Kabsch W, Wallimann T, Schlattner U. (2000). Crystal structure of human ubiquitous mitochondrial creatine kinase. *Proteins.* **39**, 216-225.
- Emsley P, Cowtan K. (2004). Coot: model-building tools for molecular

- graphics. *Acta Cryst. D.* **60**, 2126-2132.
- Fritz-Wolf K, Schnyder T, Wallimann T, Kabsch W. (1996). Structure of mitochondrial creatine kinase. *Nature.* **381**, 341-345.
- Furter R, Kaldis P, Furter-Graves E, Schnyder T, Eppenberger HM, Wallimann T. (1992). Expression of active octameric chicken cardiac mitochondrial creatine kinase in *Escherichia coli*. *Biochem. J.* **288**, 771-775.
- Goddard TD, Huang CC, Meng EC, Pettersen EF, Couch GS, Morris JH, Ferrin TE. (2018). UCSF ChimeraX: Meeting modern challenges in visualization and analysis. *Protein Sci.* **27**, 14-25.
- Gross M, Wallimann T. (1993). Kinetics of assembly and dissociation of the mitochondrial creatine kinase octamer. A fluorescence study. *Biochemistry.* **32**, 13933- 13940.
- Gross M, Furter-Graves EM, Wallimann T, Eppenberger HM, Furter R. (1994). The tryptophan residues of mitochondrial creatine kinase: roles of Trp-223, Trp-206, and Trp-264 in active-site and quaternary structure formation. *Protein Sci.* **3**, 1058-1068.
- Gross M, Wallimann T. (1995). Dimer-dimer interactions in octameric mitochondrial creatine kinase. *Biochemistry.* **34**, 6660-6667.
- Hoffman GG, Sona S, Bertin M, Ellington WR. (2006). The role of an absolutely conserved tryptophan residue in octamer formation and stability in mitochondrial creatine kinases. *Biochim. Biophys. Acta.* **1764**, 1512-1517.

- Hornemann T, Rutishauser D, Wallimann T. (2000). Why is creatine kinase a dimer? Evidence for cooperativity between the two subunits. *Biochim Biophys Acta*. **1480**, 365-373.
- Kaldis P, Furter R, Wallimann T. (1994). The N-terminal heptapeptide of mitochondrial creatine kinase is important for octamerization. *Biochemistry*. **33**, 952-959.
- Kaldis P, Wallimann T. (1995). Functional differences between dimeric and octameric mitochondrial creatine kinase. *Biochem J*. **308**, 623-7.
- Kazak L, Chouchani ET, Jedrychowski MP, Erickson BK, Shinoda K, Cohen P, Vetrivelan R, Lu GZ, Laznik-Bogoslavski D, Hasenfuss SC, Kajimura S, Gygi SP, Spiegelman BM. (2015). A creatine-driven substrate cycle enhances energy expenditure and thermogenesis in beige fat. *Cell*, **163**, 643–655.
- Khuchua ZA, Qin W, Boero J, Cheng J, Payne RM, Saks VA, Strauss AW. (1998). Octamer formation and coupling of cardiac sarcomeric mitochondrial creatine kinase are mediated by charged N-terminal residues. *J Biol Chem*. **273**, 22990-22996.
- Kuby SA, Noda L, Lardy HA. (1954). Adenosinetriphosphate-creatine transphosphorylase: I. Isolation of the crystalline enzyme from rabbit muscle. *J. Biol. Chem*. **209**, 191-201.
- Larkin MA, Blackshields G, Brown NP, Chenna R, McGettigan PA, McWilliam H, Valentin F, Wallace IM, Wilm A, Lopez R, Thompson JD, Gibson TJ, Higgins DG. (2007). Clustal W and Clustal X version 2.0.

Bioinformatics. **23**, 2947–2948.

Marcillat O, Goldschmidt D, Eichenberger D, Vial C. (1987). Only one of the two interconvertible forms of mitochondrial creatine kinase binds to heart mitoplasts. *Biochim Biophys Acta*. **890**, 233-241.

Milner-White EJ, Watts DC. (1971). Inhibition of adenosine 5'-triphosphate-creatine phosphotransferase by substrate-anion complexes. Evidence for the transition-state organization of the catalytic site. *Biochem J*. **122**, 727-740.

Müller S, Balaz M, Stefanicka P, Varga L, Amri EZ, Ukropec J, Wollscheid B, Wolfrum C. (2016). Proteomic analysis of human brown adipose tissue reveals utilization of coupled and uncoupled energy expenditure pathways. *Sci. Rep.* **6**, 30030.

Murshudov GN, Skubak P, Lebedev AA, Pannu NS, Steiner RA, Nicholls RA, Winn MD, Long F, Vagin AA. (2011). REFMAC5 for the refinement of macromolecular crystal structures. *Acta Cryst. D*. **67**, 355-367.

Nusinow DP, Szpyt J, Ghandi M, Rose CM, McDonald ER 3rd, Kalocsay M, Jané-Valbuena J, Gelfand E, Schweppe DK, Jedrychowisk M, Javad Golji, Porter DA, Rejtar T, Wang YK, Kryukov GV, Stegmeier F, Erickson B, Garraway LA, Sellers WR, Gygi SP. (2022). Quantitative proteomics of the cancer cell line encyclopedia. *Cell*. **180**, 387-402.

Okabe K, Inada N, Gota C, Harada Y, Funatsu T, Uchiyama S. (2012). Intracellular temperature mapping with a fluorescent polymeric thermometer and fluorescence lifetime imaging microscopy. *Nat Commun*.

3, 705.

Robert X, Gouet P. (2014). Deciphering Key Features in Protein Structures with the New ENDscript Server. *Nucleic Acids Research*. **42**, W320-W324.

Ruan L, Chen J, Du C, Lu H, Zhang J, Cai X, Dou R, Lin W, Chai Z, Nie G, Hu Y. (2021). Mitochondrial temperature-responsive drug delivery reverses drug resistance in lung cancer. *Bioact Mater*. **13**, 191-199.

Ryan CJ, Kennedy S, Bajrami I, Matallanas D, Lord CJ. (2017). A Compendium of co-regulated protein complexes in breast cancer reveals collateral loss events. *Cell Syst*. **5**, 399-409.

Saks VA, Ventura-Clapier R, Aliev MK. (1996). Metabolic control and metabolic capacity: two aspects of creatine kinase functioning in the cells. *Biochim. Biophys. Acta*. **1274**, 81-88.

Schlattner U & Wallimann T. (2000). Octamers of mitochondrial creatine kinase isoenzymes differ in stability and membrane binding. *J Biol Chem*. **275**, 17314-20.

Schlegel J, Zurbriggen B, Wegmann G, Wyss M, Eppenberger HM, Wallimann T. (1988). Native mitochondrial creatine kinase forms octameric structures. I. Isolation of two interconvertible mitochondrial creatine kinase forms, dimeric and octameric mitochondrial creatine kinase: characterization, localization, and structure-function relationships. *J Biol Chem*. **263**, 16942-53.

Schlegel J, Wyss M, Schurch U, Schnyder T, Quest A, Wegmann G, Eppenberger HM, Wallimann T. (1998). Mitochondrial creatine kinase

- from cardiac muscle and brain are two distinct isoenzymes but both form octameric molecules. *J. Biol. Chem.* **263**, 16963-16969.
- Streijger F, Pluk H, Oerlemans F, Beckers G, Bianco AC, Ribeiro MO, Wieringa B, Van der Zee CE. (2009). Mice lacking brain-type creatine kinase activity show defective thermoregulation. *Physiol Behav.* **97**, 76–86.
- Svensson PA, Jernås M, Sjöholm K, Hoffmann JM, Nilsson BE, Hansson M, Carlsson LM. (2011). Gene expression in human brown adipose tissue. *Int. J. Mol. Med.* **27**, 227-232.
- Wallimann T, Wyss M, Brdiczka D, Nicolay K, Eppenberger HM. (1992). Intracellular compartmentation, structure and function of creatine kinase isoenzymes in tissues with high and fluctuating energy demands: the Pphosphocreatine circuit_ for cellular energy homeostasis. *Biochem J.* **281**, 21-40.
- Wallimann T, Hemmer W. (1994). Creatine kinase in non-muscle tissues and cells. *Mol. Cell. Biochem.* **133 – 134**, 193-220.
- Watanabe M, Yamamoto T, Kakuwata R, Okada N, Kajimoto K, Yamazaki N, Kataoka M, Baba Y, Tamaki T, Shinohara Y. (2008). Synchronized changes in transcript levels of genes activating cold exposure-induced thermogenesis in brown adipose tissue of experimental animals. *Biochim. Biophys. Acta.* **1777**, 104-112.

Abstract in Korea (국문초록)

AdipoR1-P5 복합체 모델 및 미토콘드리아 크레아틴

키나제 이중 복합체의 구조 분석

빈 경 욱

자연과학대학 화학부

서울대학교 대학원

학위 논문은 주로 리간드가 어떻게 결합하는지에 대한 분자 수준의 이해를 얻고 세포 환경에서 새로운 특성을 갖는 단백질의 구조를 규명하는 데 중점을 두고 있다. 논문은 두 개의 연구 장으로 나누어져 있다.

1장에서는 아디포넥틴 수용체 1-펜타펩타이드(AdipoR1-P5) 모델의 구조 분석에 대해 논의할 것이다. AdipoR1은 GPCR 유사 수용체이며 아디포넥틴(APN)이 결합할 때 AMP 활성화 단백질 키나제 (AMPK) 신호 전달 경로를 중재한다. AdipoR1의 apo 구조는 2015년에 보고되었지만 AdipoR1-APN 복합체의 구조는 아직 규명되지 않았다. AdipoR1-APN 복합체의 구조적 정보를 바탕으로 APN과 관

련된 질병을 치료하기 위해서는 최적의 작용제를 만드는 것이 필요하지만 AdipoR1과 APN 간의 상호 작용은 아직 알려져 있지 않다. 따라서 APN이 AdipoR1에 결합하는 방식과 AdipoR1에 결합하는 APN의 결합 부위를 확인하기 위해 AdipoR1-APN 복합체 모델을 분석하였다. 본 연구에서 다중 서열 정렬 및 분자 도킹 시뮬레이션을 사용하여 내인성 APN의 원래 서열로부터 AdipoR1에 결합하는 작은 영역(P5; GLYYF)을 발견하였고, AdipoR1-P5 복합체 모델을 제공함으로써 AdipoR1에 대한 효율적인 리간드로 기능할 수 있음을 입증하였다. 이를 통해 AdipoR1과 APN 사이의 결합에 중요한 핵심 아미노산 서열을 규명했으며, 이는 AdipoR1 활성화 펩타이드를 설계하여 새로운 후보 약물을 발굴하는 전략에 적용될 수 있을 것이다.

2장에서는 미토콘드리아 크레아틴 키나제(CKMT1 및 CKMT2)의 구조적 및 기능적 연구에 대해 논의할 것이다. 본 연구는 Steven P. Gygi 박사팀이 제공한 375개의 암세포주 단백질체 데이터를 분석하는 것으로 시작되었다. 흥미롭게도 미토콘드리아에 위치한 CKMT1과 CKMT2라는 두 가지 단백질이 피어슨 상관 관계 값이 높은 것을 발견하였다. CKMT1과 CKMT2가 발현되는 조직이 서로 다른 것으로 알려져 있지만, 높은 피어슨 상관값은 두 단백질이 서로 상호작용하여 세포 내에서 생물학적 기능을 수행할 수 있음을 시사한다. 따라서 CKMT1과 CKMT2가 미토콘드리아에서 이중 복합체를 형성하여

세포내에서 어떤 기능할 것이라는 가설을 세웠다. 이에 따라 본 연구에서는 CKMT 이중복합체의 X선 결정구조를 규명하였고, 4:4 화학량론으로 팔합체를 형성함을 확인하였다. 흥미롭게도 이중 복합체가 이전에 보고된 동중 복합체와 다른 특성을 가졌으며, 특히 이중 복합체가 동중 복합체에 비해 열안정성이 더 우수하였다. 우리의 실험 데이터를 바탕으로 본 연구 결과는 높은 발현 상관 값과 높은 열 안정성을 갖는 CKMT 이중 복합체의 잠재적 형성을 나타낸다. 최근에 보고된 정량적인 단백질체학 연구에 따르면 CKMT1과 CKMT2의 단백질 발현이 열발생 지방세포에서 강력하게 증가되는 것으로 나타났다. 이러한 맥락에서 본 연구는 조직의 열 생성 환경과 관련된 중요한 생물학적 의미를 제시할 수 있다.

주요어: 아디포넥틴 수용체 1, 펜타펩타이드, 도킹 시뮬레이션, 미토콘드리아 크레아틴 키나제, X-선 결정학, 온도 안정성

학 번: 2016-20347